universität wien

MASTERARBEIT / MASTER'S THESIS

Titel der Masterarbeit / Title of the Master's Thesis

"Modelling of the Initiation of Deep Moist Convection in Relation to Upper Level Moisture Gradients"

verfasst von / submitted by

Astrid Barbara Kainz, B. Sc.

angestrebter akademischer Grad / in partial fulfilment of the requirements for the degree of

Master of Science (M. Sc.)

Wien, 2016 / Vienna 2016

Studienkennzahl lt. Studienblatt / degree programme code as it appears on the student record sheet:	A 066 614
Studienrichtung lt. Studienblatt / degree programme as it appears on the student record sheet:	Masterstudium Meteorologie
Betreut von / Supervisor:	Ao. Univ.-Prof. Mag. Dr. Leopold Haimberger

Acknowledgements

I would like to thank ao. Univ.-Prof. Dr. Haimberger for his willingness to supervise my thesis.

My sincerest thanks go to my co-supervisor Dott. Dott. ric. Stefano Serafin for supporting and guiding me through this thesis, for his help with running the WRF model, his useful ideas and comments and for his continuous feedback.

Furthermore, I want to thank Mag. Thomas Krennert from ZAMG who led me to the idea of writing my thesis in the field of interest, for the good cooperation with ZAMG, the helpful discussions and also for the provided data.

I would also like to thank Dr. Johannes Sachsperger for his support in questions related to Python.

Many thanks go to my family for supporting me in my studies, for their financial assistance and for encouraging and motivating me whenever I needed it.

Abstract

The predictability of single-cell convection in the Alpine region, especially in the absence of fronts under so called fair-weather situations, remains a challenging task for forecasters. Therefore it is important to gain knowledge about the key factors that contribute to the initiation of single-cell deep moist convection (DMC) under these conditions. Satellite studies have shown that favourable locations for the first initiation of DMC under fair-weather conditions with widespread shallow convection over mountainous terrain are water vapour gradients in the middle or upper troposphere, as of now termed UTMG (upper tropospheric moisture gradient) (Krennert and Zwatz-Meise, 2003).

Based on two WRF (Weather Research and Forecasting) hindcast simulations with three nested domains (20 km, 4 km, 800 m), the factors that may have contributed to the initiation of DMC are analysed for representative cases in the Alpine region. Therefore, different hypotheses related to UTMG are investigated with regard to their role in supporting the initiation of DMC. In particular, different types of instabilities, including moist symmetric instability (MSI), are investigated as possible mechanisms for favouring the transition from shallow to deep moist convection.

Analysis of the simulated case of 7 July 2014 reveals that the initiation of DMC can actually be related to a gradient in relative humidity at 300 hPa. Both the 4-km and 800-m domain resolve convection in reasonably good agreement with the observations. The transition from shallow to deep convection takes place in an environment characterized by negative (saturated) equivalent potential vorticity (EPV) at lower and mid-levels of the troposphere and high values of slantwise convective potential available energy (SCAPE), both of which are indicators for moist symmetric instabilities, but also gravitational instabilities. Forward trajectories have been computed to provide a better distinction between the different types of instabilities. It has turned out that there is no clear evidence for a contribution of MSI to the evolution of DMC regarding the chosen model and settings. Here, the vertical wind component seems to dominate the horizontal wind components within the convective updraught at any time.

A second simulated case (21 July 2013) shows that the convection is again resolved by the model. In this case the first initiation of DMC is not clearly related to the UTMG and convection is generally more widespread. The strongest gradient in relative humidity is found at lower levels, i.e. at 400 hPa, the gradients being generally lower as compared to case 1. Indicators for MSI in terms of negative EPV and SCAPE are much weaker and can not be clearly connected to the area where DMC was initiated.

Zusammenfassung

Die Vorhersagbarkeit von Einzelzellgewittern im Alpenraum, insbesondere in Abwesenheit von Fronten unter sogenannten Schönwetterbedingungen, gestaltet sich als schwierige Aufgabe für Meteorologen. Umso wichtiger ist es, das Wissen über Faktoren, die zur Initiierung von hochreichender Feuchtekonvektion (deep moist convection, DMC) unter solchen Umgebungsbedingungen beitragen, stets zu verbessern. Fallstudien mit Satellitenbildern haben gezeigt, dass Feuchtegradienten in der mittleren oder oberen Troposphäre (upper tropospheric moisture gradients, UTMG) eine bevorzugte Lage für die erste Initiierung von DMC unter Schönwetterbedinungen bei weitverbreiteter flacher Konvektion über dem Gebirge darstellen. (Krennert and Zwatz-Meise, 2003).

Anhand von zwei WRF-Simulationen mit drei genesteten Domänen (20 km, 4 km, 800 m) werden Faktoren, die zur Initiierung von DMC beigetragen haben könnten, für zwei repräsentative Fälle im Alpenraum analysiert. Dazu werden verschiedene Hypothesen im Zusammenhang mit UTMG und deren Rolle bei der Initiierung von DMC untersucht. Ein wesentlicher Teil besteht darin, verschiedene Instabilitäten zu untersuchen, einschließlich der feucht-symmetrischen Instabilität (moist symmetric instability, MSI) als mögliche begünstigende Ursache für den Übergang von flacher zu hochreichender Konvektion.

Die Ergebnisse der ersten Fallstudie vom 7. Juli 2014 zeigen, dass die Initiierung von DMC tatsächlich in Zusammenhang mit einem Gradienten der relativen Feuchte in 300 hPa auftritt. Sowohl die 4-km, als auch die 800-m Domäne erweisen sich als konvektionsauflösend und in guter Übereinstimmung mit den Beobachtungen. Zudem stellt sich heraus, dass die Umgebung beim Übergang von flacher zu hochreichender Konvektion von Bereichen negativer (gesättigter) potentieller Vorticity in der unteren bis mittleren Troposphäre und hohen SCAPE-Werten (slantwise convective available potential energy) geprägt ist, die beide Indikatoren für symmetrische, jedoch auch statische Instabilität sind. Für eine bessere Abgrenzung dieser beiden Instabilitäten wurden Trajektorien berechnet. Es hat sich herausgestellt, dass es unter Verwendung des gewählten Modells keinen eindeutigen Hinweis auf eine begünstigende Rolle von MSI auf die Entwicklung hochreichender Konvektion gibt, da die Größenordnung der vertikalen Windkomponente jene der beiden horizontalen Windkomponenten im Aufwindbereich zu jeder Zeit übertrifft.

Die Ergebnisse der zweiten Fallstudie zeigen zwar, dass die Konvektion wieder entsprechend gut aufgelöst wird, jedoch zeigt sich die konvektive Aktivität mehr verbreitet als dies in den Satellitenbildern der Fall ist. Zudem ist der Gradient der relativen Feuchte vergleichsweise schwächer ausgeprägt. Auch die Indikatoren für symmetrische Instabilität (negative EPV, SCAPE) sind in Zusammenhang mit der Initiierung von DMC nur wenig bedeutsam.

Contents

Chapter 1

Introduction

1.1 Motivation

Single-cell or pulse convection represents about 30 percent of summertime thunderstorm activity in the Eastern Alpine Region (Krennert and Zwatz-Meise, 2003). The predictability of such events remains a challenge to forecasters, especially in the presence of orography, hence the understanding of the mechanisms of storm initiation remains an important task in order to improve the quality of forecasts. Satellite studies have shown that upper tropospheric moisture gradients (UTMG) are often favourable locations for the initiation of deep moist convection (Krennert and Zwatz-Meise, 2003). The goal of this thesis is to find the responsible mechanisms for the initiation of single-cell convection along UTMG by performing hindcast simulations for representative cases in the Alpine region with the WRF (Weather Research Forecasting) model and analysing relevant diagnostic parameters. Simulation results are compared to observed satellite images.

1.2 Thesis Organization

Chapter 2 deals with different types of mesoscale instabilities relevant for the initiation of deep moist convection. In this context, the concept of symmetric instabilities is introduced. Diagnostic parameters for moist convective and moist symmetric instability are discussed and the mechanisms of the initiation of deep moist convection in terms of an ingredient-based methodology are presented. Finally, the characteristics of different types of convective storms are briefly discussed. In Chapter 3 previous literature attributing characteristics of UTMG is reviewed and different hypotheses for the initiation of DMC in relation to UTMG are presented. In Chapter 4 and 5 case studies are presented, analysing the previous concepts by performing WRF simulations and comparing the results to satellite images. An attempt is made to link the initiation of deep moist convection to upper level moisture gradients. Finally, Chapter 6 summarizes the results.

Chapter 2

Theoretical Background

2.1 Types of Mesoscale Instabilities

"Instability is defined as a property of the steady state of a system such that certain disturbances introduced into the steady state will increase in magnitude, with the maximum perturbation amplitude always remaining larger than the initial amplitude." (American Meteorological Society, 2016b)

Meteorological phenomena cover a broad range of different horizontal scales and time scales. Deep moist convection is a mesoscale phenomenon, whereby according to Orlanski (1975) the mesoscale covers a horizontal range of 2 - 2000 km. Instability can be considered as one of the major ingredients for the initiation of deep moist convection (see section 1.2.6). Compared to the synoptic scale, which includes large-scale weather phenomena that are basically driven by baroclinic instability, a wide variety of instabilities operates on the mesoscale. Therefore, the following chapter treats a few mesoscale instabilities that are related to deep moist convection.

2.1.1 Gravitational Instability

Gravitational instability, sometimes referred to as *static instability*, is characterized by the vertical displacement of an air parcel due to density differences between the parcel and its environment with buoyancy acting as driving force. The release of gravitational instability leads to *upright convection* or *gravitational convection*. The quantitative description of gravitational instability is based on parcel theory, i.e., on the assumption that there is no mass exchange between a lifted air parcel and the surrounding environment and that the parcel immediately adjusts to the pressure of the surrounding atmosphere. It is useful to start with the vertical momentum equation (Lin, 2007, p. 238 ff):

$$\frac{\mathrm{dw}}{\mathrm{dt}} = \mathrm{g}\left(\frac{\mathrm{T}-\overline{\mathrm{T}}}{\mathrm{T}}\right) \equiv \mathrm{B} \tag{2.1}$$

where B is the buoyancy force, $\overline{\mathrm{T}}$ is the temperature of the environment and T the temperature of the considered air parcel. Friction, Coriolis force and pressure gradient force are neglected in this case and the motion of the air parcel only depends on the buoyancy force. The parcel is

now displaced vertically from its initial equilibrium position by a distance Δz. The governing equation for Δz can be derived from Eq. 2.1, and is:

$$\frac{d^2\Delta z}{dt^2} + N^2\Delta z = 0 \tag{2.2}$$

where N is referred to as the Brunt-Väisälä frequency:

$$N^2 = \frac{g}{\overline{\Theta}}\frac{\partial\overline{\Theta}}{\partial z} = \frac{g}{T}(\Gamma_d - \gamma) \tag{2.3}$$

Here, Θ is potential temperature, Γ_d is the dry adiabatic lapse rate and γ the environmental lapse rate. The criteria for static instability for dry air are as follows:

$$\frac{\partial\overline{\Theta}}{\partial z}\begin{cases} > 0 & \textit{absolutely stable} \quad (N^2 > 0, \gamma < \Gamma_d) \\ = 0 & \textit{dry statically neutral} \quad (N^2 = 0, \gamma = \Gamma_d) \\ < 0 & \textit{dry statically unstable} \quad (N^2 < 0, \gamma > \Gamma_d) \end{cases}$$

Thus, the buoyancy force acts as a restoring force in a statically stable atmosphere (a vertically displaced air parcel returns back to its initial position and oscillates vertically) while in a statically unstable atmosphere an air parcel accelerates away from its initial position.

If the atmosphere is considered to be saturated, the *saturated moist Brunt-Väisälä frequency* N_m must be used (Lin, 2007, p. 242):

$$N_m^2 = \left(\frac{1}{1+q_w}\right)\left\{\left[\frac{\Gamma_s(c_p + c_l q_w)}{\overline{\Theta}_e}\right]\frac{\partial\overline{\Theta}_e}{\partial z} - \left[g - \Gamma_s c_l\frac{\overline{\Theta}_e}{\overline{T}}\right]\frac{\partial q_w}{\partial z}\right\} \tag{2.4}$$

where Θ_e is the equivalent potential temperature, Γ_s is the saturated adiabatic lapse rate, c_l is the specific heat capacity at constant pressure of liquid water, c_p is the specific heat capacity of dry air at constant pressure and q_w is the total water mixing ratio. Θ_e can be approximately computed as:

$$\Theta_e = \Theta \exp\left\{\frac{L q_v}{c_p T_{LCL}}\right\} \tag{2.5}$$

where L is the latent heat of condensation, q_v is the water vapor mixing ratio and T_{LCL} is the temperature at the lifting condensation level (Lin, 2007, p. 242). Θ_e corresponds to the temperature an air parcel would have if all its water vapor were condensed and the resulting latent heat warmed the parcel.

So the criteria for moist static instability can be obtained by replacing the Brunt-Väisälä frequency N in Eq 2.2 with the saturated moist Brunt-Väisälä frequency N_m. Moist absolute instability occurs if $N_m^2 < 0$ or $\gamma_s > \Gamma_s$. Eq. 2.4 yields that this is equivalent to $\frac{\partial\overline{\Theta}_e}{\partial z} < 0$ only if

q_w remains constant with height (Lin, 2007, p. 242).

If the parcel is unsaturated at first but becomes saturated when it is lifted upward, *conditional instability* can be present. This is the case when the environmental lapse rate γ is less than the dry adiabatic lapse rate but greater than the saturated adiabatic lapse rate: $\Gamma_s < \gamma < \Gamma_d$. Another criterion for conditional instability can be presented in terms of the vertical gradient of the *saturated equivalent potential temperature*:

$$\Theta_e^* = \Theta \exp\left\{\frac{L q_{vs}}{c_p T}\right\} \tag{2.6}$$

where Θ_e^* is defined as the equivalent potential temperature assuming that the atmosphere is initially saturated, L is the latent heat of condensation and q_{vs} is the saturation mixing ratio of water vapour (Lin, 2007, p. 245).

$$\frac{\partial \overline{\Theta}_e^*}{\partial z} \begin{cases} > 0 & \textit{conditionally stable} \\ = 0 & \textit{conditionally neutral} \\ < 0 & \textit{conditionally unstable} \end{cases}$$

If an atmospheric *layer* becomes statically unstable after being lifted, the atmospheric state is said to be *potentially unstable* or *convectively unstable*. In such a layer, the top cools quickly at the dry adiabatic lapse rate while the bottom cools slowly at the moist adiabatic lapse rate and therefore the atmosphere becomes destabilized. The criteria for potential instability can be expressed in terms of equivalent potential temperature:

$$\frac{\partial \overline{\Theta}_e}{\partial z} \begin{cases} > 0 & \textit{potentially stable} \\ = 0 & \textit{potentially neutral} \\ < 0 & \textit{potentially unstable} \end{cases}$$

A layer which is potentially unstable does not necessarily need to be conditionally unstable and vice versa as illustrated in Fig. 2.1. The left frame shows a conditionally unstable area between 750 and 500 hPa, approximately, i.e. Θ_e^* decreases with height, whereas no unstable area can be identified in the right frame, where Θ_e increases with height.

2.1.2 Inertial Instability

While for static instabilities an air parcel is displaced and accelerated vertically, inertial instability is characterized by horizontal acceleration away from an equilibrium position. When inertial stability is present, the Coriolis force acts as a restoring force. Considering an air parcel that

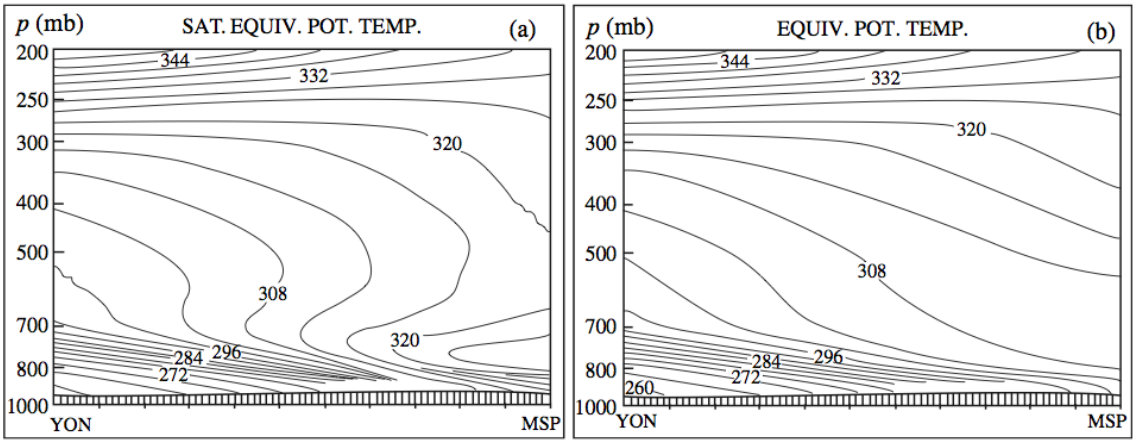

Figure 2.1: 9-h forecast by Rapid Update Cycle (RUC) valid for 00:00 UTC 3 Jan 1998. Cross Section from Dauphin, Manitoba(YON) to Minneapolis-St. Paul, Minnesota (MSP): (a) Saturated equivalent potential temperature Θ_e^* and (b) equivalent potential temperature Θ_e, from Schultz and Schumacher (1999)

is moving with the zonal geostrophic wind, it is useful to start with the horizontal equations of motion, following Holton and Hakim (2012):

$$\frac{\mathrm{du}}{\mathrm{dt}} = \mathrm{fv} = \mathrm{f}\frac{\mathrm{dy}}{\mathrm{dt}} \tag{2.7}$$

$$\frac{\mathrm{dv}}{\mathrm{dt}} = \mathrm{f}(\mathrm{u_g} - \mathrm{u}) \tag{2.8}$$

where u and v are the actual wind components, $\mathrm{u_g}$ the geostrophic wind component and f the Coriolis parameter. If an air parcel is now displaced horizontally by a distance $\Delta\mathrm{y}$, its new zonal velocity and the geostrophic wind are:

$$\mathrm{u} = \mathrm{u_0} + \mathrm{f}\Delta\mathrm{y} \tag{2.9}$$

$$\mathrm{u_g} = \mathrm{u_0} + \frac{\partial \mathrm{u_g}}{\partial \mathrm{y}}\Delta\mathrm{y} \tag{2.10}$$

Eq. 2.8 can then be rewritten as:

$$\frac{\mathrm{dv}}{\mathrm{dt}} = \frac{\mathrm{d}^2\Delta\mathrm{y}}{\mathrm{dt}^2} = -\mathrm{f}\left(\mathrm{f} - \frac{\partial \mathrm{u_g}}{\partial \mathrm{y}}\right)\Delta\mathrm{y} = -\mathrm{f}\frac{\partial \mathrm{M}}{\partial \mathrm{y}}\Delta\mathrm{y} \tag{2.11}$$

$\mathrm{M} \equiv \mathrm{fy} - \mathrm{u_g}$ being the absolute geostrophic momentum. Analogously to the criteria for static instability, criteria for inertial instability can be determined:

$$f\frac{\partial \overline{M}}{\partial y} \begin{cases} > 0 & \textit{stable} \\ = 0 & \textit{neutral} \\ < 0 & \textit{unstable} \end{cases}$$

Eq. 2.11 also shows that in the Northern Hemisphere ($f > 0$), the absolute vorticity $\left(f - \frac{\partial u_g}{\partial y}\right)$ is positive for an inertially stable flow.

2.1.3 Symmetric Instability

Symmetric instability may occur in an atmosphere that is statically and inertially stable. Under these conditions, an air parcel may be accelerated away from its original position if it is displaced along a slantwise path.

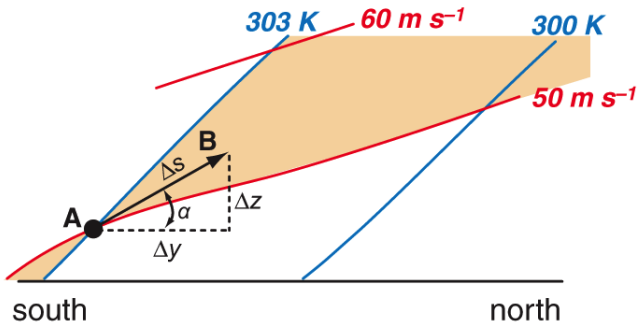

Figure 2.2: Schematic cross section of isentropic (blue) and momentum surfaces (red) under symmetrically unstable conditions (Markowski and Richardson, 2011)

To provide a better understanding of the concept of symmetric instability, it is useful to demonstrate it with a schematic sketch, as illustrated by Fig. 2.2. Consider a (dry) statically and inertially stable configuration of the atmosphere. An air parcel, initially positioned at A, that is displaced along a slantwise path towards B, experiences a vertical restoring force and a horizontal restoring force. When the $\overline{\Theta}$ surfaces are sloped more steeply than the $\overline{M}$ surfaces, a net acceleration occurs along the slanted path towards the direction of displacement, leading to dry symmetric instability. This concept is also called the $\overline{M} - \overline{\Theta}$ *relationship* (Schultz and Schumacher, 1999). It follows that a necessary condition for dry symmetric instability is (Lin, 2007):

$$\left|\frac{\partial z}{\partial y}\right|_{\overline{\Theta}} > \left|\frac{\partial z}{\partial y}\right|_{\overline{M}} \tag{2.12}$$

Analogously, dry symmetric instability can be viewed as dry gravitational instability on an $\overline{M}$

surface or inertial instability on a $\overline{\Theta}$ surface (Markowski and Richardson, 2011):

$$\left(\frac{\partial\overline{\Theta}}{\partial \mathrm{z}}\right)_{\overline{\mathrm{M}}} < 0 \tag{2.13}$$

$$\left(\frac{\partial\overline{\mathrm{M}}}{\partial \mathrm{y}}\right)_{\overline{\Theta}} > 0 \tag{2.14}$$

In a strict sense, symmetric instability should be determined by hydrostatically and geostrophically balanced mean states $\overline{\Theta}$ and $\overline{\mathrm{M}}$ (Xu, 1986). In assessing dry symmetric instability, $\overline{\Theta}$ may be replaced by an observed potential temperature profile Θ while replacing $\overline{\mathrm{M}}$ by an observed momentum profile M is generally a poor approximation (Schultz and Schumacher, 1999, p. 2713). Nevertheless, when using mesoscale model data, the geostrophic wind is often much noisier than the total wind and some researchers and forecasters tend to approximate $\overline{\mathrm{M}}$ by M (Schultz and Schumacher, 1999, p. 2712).

Considering a moist atmosphere, criteria for *conditional symmetric instability* (CSI) and *potential symmetric instability* (PSI) can be determined analogously to the criteria for static instability by applying parcel and layer theories: CSI and PSI occur where $\left(\frac{\partial\overline{\Theta}^{*}_{\mathrm{e}}}{\partial \mathrm{z}}\right)_{\overline{\mathrm{M}}} < 0$ and $\left(\frac{\partial\overline{\Theta}_{\mathrm{e}}}{\partial \mathrm{z}}\right)_{\overline{\mathrm{M}}} < 0$, respectively (Schultz and Schumacher, 1999, p. 2713). Moist symmetric instability (MSI) is a general term for CSI *or* PSI.

2.1.4 Coexistence of Instabilities

Moist gravitational instability (CI/PI) is often observed in the surroundings of moist symmetric instability (CSI/PSI), as illustrated by Fig. 2.3, which shows stability regimes occurring at the same time across a frontal environment. At this point, it should be mentioned that CI/PI is a special case of CSI/PSI in which $\Theta^{*}_{e}/\Theta_{e}$ surfaces are not only sloped more steeply than $\overline{\mathrm{M}}$ surfaces but are also overturned (Schultz and Schumacher, 1999, p. 2718).

The coexistence of CI/PI and CSI/PSI may lead to both gravitational and slantwise convection and is sometimes referred to as *convective-symmetric instability* (Emanuel, 1980). Compared to gravitational convection, slantwise convection is usually assumed to be weaker, i.e. in the order of tens of cms^{-1} to a few ms^{-1} (Schultz and Schumacher, 1999, p. 2721). Furthermore, Bennetts and Sharp (1982) found that when both instabilities coexist, gravitational instability tends to dominate in time, caused by a larger growth rate of gravitational instability compared to symmetric instability (Bennetts and Sharp, 1982).

According to Xu (1986) and his studies of mesoscale rainbands there are two possible mechanisms for the coexistence of CI/PI and CSI/PSI. The first is called *upscale development* and is characterized by small scale moist gravitational convection followed by the release of symmetric instability and, as a result, mesoscale banded organization of clouds. The second mechanism, the

so called *downscale development*, refers to slantwise convection under moist symmetrically unstable conditions leading to the release of latent heat and a destabilization of the mid-troposphere. This consequently induces gravitational convection. These two mechanisms are illustrated in Fig. 2.4.

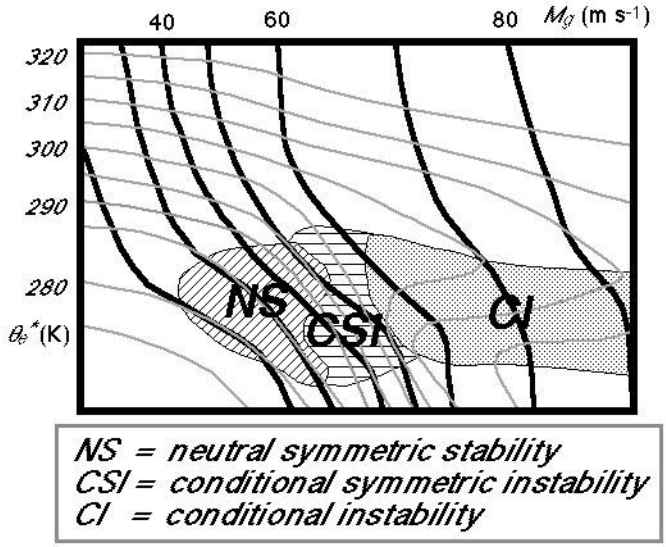

Figure 2.3: Coexistence of Instabilities: CI = Conditional Instability, CSI = Conditional Symmetric Instability, NS = Neutral Symmetric Stability (Schultz and Schumacher, 1999)

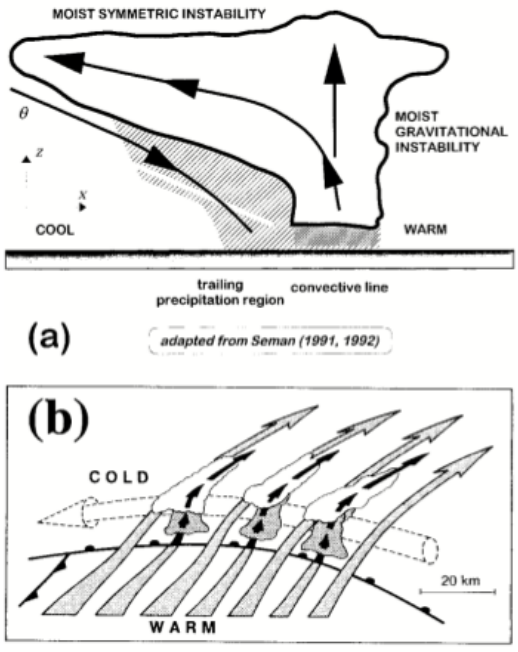

Figure 2.4: (a) Cross section of upscale convective-symmetric instability in a mesoscale convective system (adapted from Seman (1991) and Seman (1992)), (b) downscale convective-symmetric instability (adapted from Neiman et al. (1993), after Schultz and Schumacher (1999))

2.1.5 Diagnostic Parameters for CI/CSI

a) Equivalent Potential Vorticity

Assessing moist symmetric instabilities, i.e. CSI/PSI based on the $\overline{\mathrm{M}} - \overline{\Theta}_{\mathrm{e}}^{*}/\overline{\mathrm{M}} - \overline{\Theta}_{\mathrm{e}}$ *relationship* has its limitations because several assumptions are required for determining regions of moist symmetric instabilities: First, the geostrophic wind is assumed to be constant in the alongfront direction; second, the cross section of the $\overline{\mathrm{M}}$ and $\overline{\Theta}_{\mathrm{e}}^{*}/\overline{\Theta}_{\mathrm{e}}$ isolines has to be perpendicular to the vertical geostrophic wind shear; third, the geostrophic wind has to be an appropriate approximation for the basic state (Schultz and Schumacher, 1999).

In a different approach the three-dimensional *geostrophic potential vorticity PV* is used for diagnosing regions of dry symmetric instability (Hoskins, 1974):

$$\mathrm{PV} = \mathrm{g}\eta_{\mathrm{g}}\nabla\Theta \tag{2.15}$$

where η_g is the three-dimensional geostrophic absolute vorticity vector and ∇ is the three-dimensional nabla operator. If $\mathrm{PV} < 0$, dry symmetric instability is present, assuming that gravitational and inertial instabilities are absent (Schultz and Schumacher, 1999, p. 2715). Analogously, PSI or CSI occur when the *equivalent geostrophic potential vorticity* ($\mathrm{EPV} = \mathrm{g}\eta_{\mathrm{g}}\nabla\Theta_{\mathrm{e}}$) or *saturated equivalent geostrophic potential vorticity* ($\mathrm{EPV_s} = \mathrm{g}\eta_{\mathrm{g}}\nabla\Theta_{\mathrm{e}}^{*}$) are negative, respectively. The fact that EPV can be computed directly from NWP (Numerical Weather Prediction) model output in its three-dimensional form, makes it a more convenient tool for assessing MSI, because it doesn't depend on a cross-section orientation and furthermore, it can be computed on horizontal maps.

McCann (1995) presented a method for computing three-dimensional equivalent potential vorticity from model output on pressure coordinates. Starting from a definition of EPV, calculated on pressure surfaces:

$$\mathrm{EPV} = -\mathrm{g}\eta_{\mathrm{g}}\nabla\Theta_{\mathrm{e}} \tag{2.16}$$

McCann (1995) suggested to expand each of these vectors into three dimensions, yielding:

$$\mathrm{EPV} = \mathrm{g}\left[\frac{\partial\Theta_{\mathrm{e}}}{\partial\mathrm{x}}\frac{\partial\mathrm{v_g}}{\partial\mathrm{p}} - \frac{\partial\Theta_{\mathrm{e}}}{\partial\mathrm{y}}\frac{\partial\mathrm{u_g}}{\partial\mathrm{p}} - \left(\frac{\partial\mathrm{v_g}}{\partial\mathrm{x}}\frac{\partial\mathrm{u_g}}{\partial\mathrm{y}} + \mathrm{f_k}\right)\frac{\partial\Theta_{\mathrm{e}}}{\partial\mathrm{p}}\right] \tag{2.17}$$

which can be easily evaluated on model output data.

Despite the advantages of using EPV as diagnostic tool (it doesn't require the strict assumptions made in the $\overline{\mathrm{M}} - \overline{\Theta}_{\mathrm{e}}^{*}$ *relationship*) it should be mentioned that negative EPV/EPV$_s$ may also indicate regions of PI/CI. Therefore, additional analysis regarding moist gravitational and inertial instabilities is necessary (Schultz and Schumacher, 1999, p. 2718).

b) CAPE, CIN and SCAPE

Convective available potential energy (CAPE) is defined as the total amount of energy available from buoyancy or alternatively as the work done by buoyancy in lifting an air parcel from its *level of free convection* (LFC) to its *equilibrium level* (EL):

$$\mathrm{CAPE} = \int_{\mathrm{LFC}}^{\mathrm{EL}} \mathrm{B}\ \mathrm{dz} \tag{2.18}$$

In contrast, the *convective inhibition* quantifies the amount of energy that prevents an air parcel from reaching its LFC (starting from an initial position z_0):

$$\mathrm{CIN} = -\int_{z_0}^{\mathrm{LFC}} \mathrm{B}\ \mathrm{dz} \tag{2.19}$$

Slantwise convective available potential energy (SCAPE) can be defined as the maximum kinetic energy that is available from CSI, consisting of both horizontal and vertical motions (Lin, 2007, p. 261):

$$\mathrm{SCAPE} = \int_{\mathrm{LFC}}^{\mathrm{EL}} \mathrm{g}\frac{\Theta_{\mathrm{e}}^{*} - \overline{\Theta}_{\mathrm{e}}^{*}}{\overline{\Theta}_{\mathrm{e}}^{*}}\mathrm{dz}_{\overline{\mathrm{M}}} \tag{2.20}$$

Emanuel (1983) presented a two-dimensional method for calculating slantwise convective available potential energy by analysing temperature and moisture profiles along surfaces of absolute momentum, treating them as if they were vertical. Furthermore, Shutts (1990) extended this method into three dimensions which allows for the use of SCAPE charts in the same way as one might use CAPE. In this case, SCAPE is calculated by computing CAPE along an intersection of the isosurfaces of the horizontal components of absolute geostrophic momentum (M and N). Note that in this case N should not be confused with the Brunt-Väisälä frequency.

Dixon (1999) presented a mechanism for calculating SCAPE from model output, strongly following the method of Shutts (1990). However, he recommends the use of geostrophic winds when calculating the momentum, while Shutts (1990) suggests that using the full model wind is justifiable if the geostrophic wind is too noisy.

The absolute (geostrophic) momentum consists of two components which can be derived directly from gridded data:

$$\mathrm{M_g} = \int \mathrm{f dx} + \mathrm{v_g} \tag{2.21}$$

$$\mathrm{N_g} = \int \mathrm{f dy} - \mathrm{u_g} \tag{2.22}$$

The calculation of SCAPE is typically started from the 950 hPa level because the surface values for $\mathrm{M_g}$ and $\mathrm{N_g}$ might be affected by turbulence and boundary layer schemes (Shutts, 1990). Θ

and M are read from 50 hPa pressure levels between 950 hPa and 200 hPa. SCAPE is then calculated along the intersection of M and N surfaces. The intersection is determined by finding the minimum value at each level:

$$\mathrm{MN_{min}} = (\mathrm{M_g} - \mathrm{M_0})^2 + (\mathrm{N_g} - \mathrm{N_0})^2 \tag{2.23}$$

where $\mathrm{M_0}$ and $\mathrm{N_0}$ refer to initial values at 950 hPa.

Furthermore, at each gridpoint with the nearest values of $\mathrm{M_g}$ and $\mathrm{N_g}$, the values of temperature and specific humidity are calculated and the resulting slantwise profile is read into a CAPE routine.

Gray and Thorpe (2001) presented an alternative way of calculating SCAPE by computing parcel trajectories. Generally little research has be done dealing with the use of SCAPE so its relevance as a diagnostic tool for CSI/PSI is still under debate.

2.2 Mechanisms of Initiation of Deep Moist Convection

Convection is defined as "[...]mass motions within a fluid resulting in transport and mixing of the properties of that fluid." (American Meteorological Society, 2016a). In meteorology convection generally refers to a transport of heat and moisture along an upward direction. Convection in the atmosphere occurs in different forms, it can be either *dry* (i.e. no conversion of water vapour to liquid water takes place while the air parcel is displaced vertically) or *moist* (i.e. the air parcel becomes saturated during the ascent). *Shallow convection* refers to turbulent air motions confined to the lower troposphere (usually the boundary layer), whereas *deep convection* can extend up to the tropopause.

A further distinction can be made between *free* or *forced convection*. While forced convection requires air masses being lifted through some dynamical mechanisms like frontal or orographic lifting, free convection is a result from lifting due to the presence of instability (either gravitational or symmetric) only.

Markowski and Richardson (2011) define deep moist convection as a phenomenon where air is lifted to saturation and experiences positive buoyancy, resulting in upward vertical acceleration. This requires air parcels to reach their LFC. The updraught can extend up to high levels in the troposphere.

According to the *ingredient-based methodology* three conditions are necessary in order to initiate deep moist convection (Doswell III, 1987):

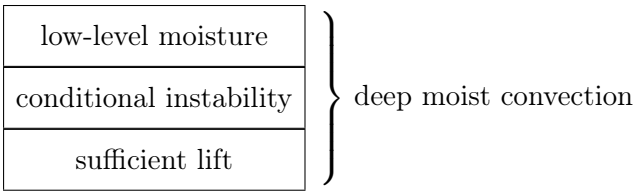

Doswell III (1987, p. 7) states, "Remove any one of these and there well may be some important weather phenomena, but the process is no longer deep, moist convection." This ingredient-based methodology can be adapted to moist slantwise convection in replacing *conditional instability* with *conditional symmetric instability* (Schultz and Schumacher, 1999, p. 2711).

2.3 Different Types of Convective Storms

Convective storms can be classified as *single-cell storms*, *multicell storms* and *supercell storms*. The characteristics of these three types are introduced shortly.

2.3.1 Single-cell storms

A single cell (also referred to as *air mass thunderstorm* or *pulse convection*) represents the most basic form of a convective storm. It consists of only one single updraught and has a lifetime of approximately 30 minutes. The life cycle of a single-cell storm consists basically of three stages which are illustrated in Fig. 2.5. The *developing stage* (a) is characterized by one or more cumuli towers which consist of strong primarily upward motions. Precipitation may form as raindrops in the upper part of the cloud, however, significant rainfall is unlikely to occur. The *mature stage* (b) is associated with both upward and downward motions. The cloud continues to grow and precipitation particles start to fall into the subcloud layer. The updraughts start to span the depth of the troposphere, followed by the overshooting of the updraught air into the stratosphere and the formation of an anvil. Due to weak vertical wind shear hydrometeors fall directly into the updraught leading to a downdraught and consequently to a replacement of the initially warm, moist air and a suppression of additional updraughts. This is called the *dissipating stage* (c) (Lin, 2007).

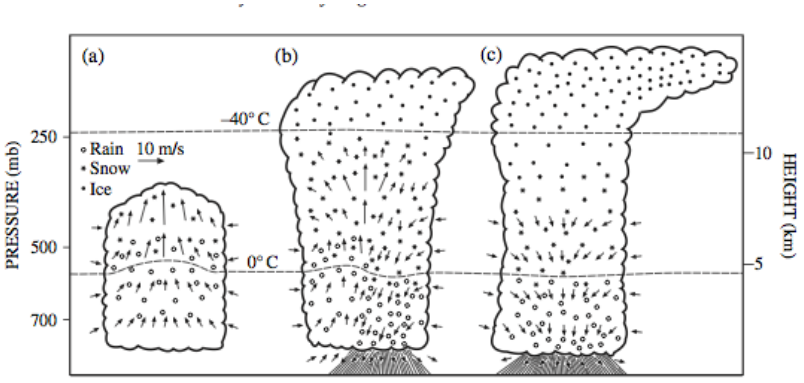

Figure 2.5: The life cycle of a single-cell storm: (a) developing stage, (b) mature stage, (c) dissipating stage (Lin (2007), adapted from Byers and Braham (1949))

2.3.2 Multicell storms

A multicell storm consists of two or more convective single cells at various stages of development. Compared to a single-cell storm, multicell storms form in the presence of stronger vertical wind shear. New cells tend to form along the leading edge of the cold pool of a pre-existing cell, which is also called *gust front*. The individual cells are short-lived while the overall multicell system may last for several hours. Multicell storms are usually more intense than single-cells and are more likely accompanied by severe weather like heavy rainfall, downbursts, hail and tornadoes. A schematic sketch of the development of a multicell is shown in Fig. 2.6.

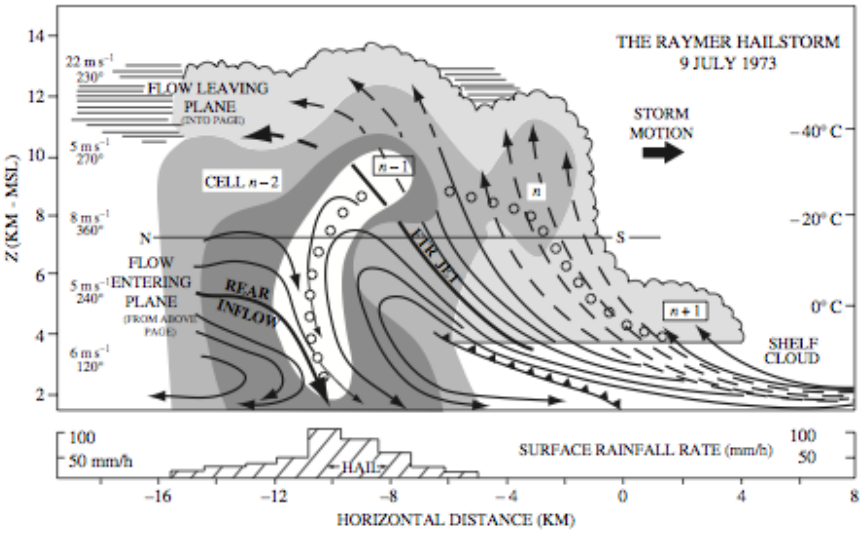

Figure 2.6: Schematic evolution of a multicell storm (Lin, 2007), adapted from Browning (1976)

2.3.3 Supercell storms

Supercell storms are the most intense type of convective storms. They can persist for several hours (due to strong vertical wind shear) and are associated with an embedded mesocyclone. Compared to multicell storms they consist of only one single updraught-downdraught pair. Supercell storms are often accompanied by severe weather like tornadoes or damaging hail. Since the present work deals with airmass or pulse convection, the exact mechanisms for the development of supercells will not be discussed further.

Chapter 3

Previous Case Studies and Hypotheses

Before the model results are presented and analysed in detail, some characteristics of UTMG are discussed based on previous studies. An attempt is made to argue for a link between these concepts and the initiation of DMC. Furthermore, the results of a satellite imagery study are presented, which played an important role in motivating the present study.

3.1 Convective initiation in relation to water vapour boundaries in satellite images - an observational study

UTMG correspond to moisture gradients in the water vapour satellite imagery where they are marked as "dark zones" or "black stripes". Krennert and Zwatz-Meise (2003) studied the initiation of DMC under fair weather conditions, i.e. in the absence of fronts, based on water vapour (WV) satellite images. They investigated about 700 cells within 50 fair-weather situations over Europe in 1999 - 2000. In 66 % of all considered cases the first appearance of DMC - detected by the 5.7 – 7.1 µm WV channel - could be connected to the boundaries of the WV gradients, i.e. to a transition zone between high and low pixel values. Before DMC occurrence, widespread shallow convection was present over mountainous terrain in the visible and infrared (IR) channels. Furthermore, it was found that the convective cells were initiated according to a diurnal cycle and developed much faster than their related WV features (Krennert and Zwatz-Meise, 2003, p. 360f.).

Investigation of the vertical stratification of the considered cases revealed that the area in the vicinity of the UTMG is characterized by conditional instability, although sometimes interrupted by weak inversions, in the lower and middle troposphere. An example for a typical stratification profile is depicted in Fig. 3.1a which corresponds to a fair-weather case in relation to the initiation of DMC on 5 June 2000. A thin absolutely unstable layer near the surface enhances the possibility of spontaneous convective overturning.

Fig. 3.1b shows the vertical profile of relative humidity within the upper level dry zone which is representative for all investigated cases. Apparently, there is a humidity maximum at 800 hPa and a distinct vertical gradient between 600 and 400 hPa. These vertical gradients in relative humidity lead to spatial variability in potential instability.

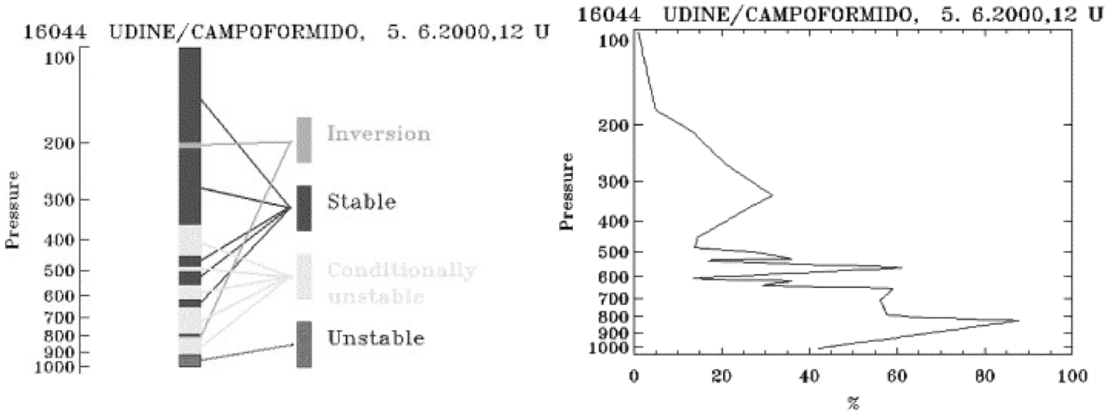

Figure 3.1: Vertical profile of relative humidity and vertical stability analysis, based on a radio sounding of Udine on 5th June 2000, 12:00 UTC (Krennert and Zwatz-Meise, 2003)

3.2 Characteristics of UTMG

UTMG can be related to dynamic processes in the middle or upper troposphere on a synoptic scale. The brighter/darker regions are associated with ascending/descending motions as well as regions of lower/higher potential vorticity (Browning, 1993). These features and their related dynamical processes have been discussed from various perspectives in previous literature, although most of them usually refer to UTMG associated with cyclonic processes, i.e. extratropical cyclones. Different names are given to these features, i.e. dry intrusion, tropopause folding, potential vorticity anomaly etc. In the following some of these concepts are introduced.

Browning (1997) studied the development of extra-tropical cyclones in relation to *dry intrusions*. He defined these dry intrusions as "[...]a coherent region of air descending from near tropopause-level." He emphasized the importance of two properties of dry intrusions, namely high potential vorticity and low wet-bulb potential temperature in different parts of the intrusion.

The impact of upper-level *PV anomalies* - which are associated with dry intrusions - on reducing gravitational stability was studied in detail by Hoskins et al. (1985). They emphasized that the convective destabilization is a consequence of vertical displacements of isentropic surfaces in the troposphere, which can contribute to the onset of convection.

According to Appenzeller et al. (1996), many mesoscale flow features at the tropopause are related to specific patterns in the lower troposphere and evolve from *stratospheric intrusions*. Detection of these features is based on high values of potential vorticity and ozone concentration and low values of water vapour. Furthermore, these intrusions can be fragmented or advected, or more precisely, they can develop into elongated streamers and subsequently roll up.

Antonescu et al. (2013) published a five-year radar-based climatology of *tropopause folds* and convective storms over Wales, United Kingdom. A tropopause fold is a further name for intrusions of stratospheric air into the troposphere, carrying high values of PV, high values of ozone mixing ratio and low relative humidity (Antonescu et al., 2013, p. 1694). It was found out that tropopause folds can either suppress or promote convection:

- Entrainment associated with dry intrusions can suppress convection as it leads to negative buoyancy due to evaporation.
- Static stability is characteristic of the stratosphere and leads to convective inhibition.
- Lift is favoured by the advection of potential vorticity (Hoskins et al., 1985).

Using a MST radar Antonescu et al. (2013) also found that an increasing vertical wind shear could be connected to tropopause folds.

In the following three hypotheses for the initiation of deep moist convection in relation to UTMG are listed and discussed.

3.3 The role of moist symmetric instability (MSI)

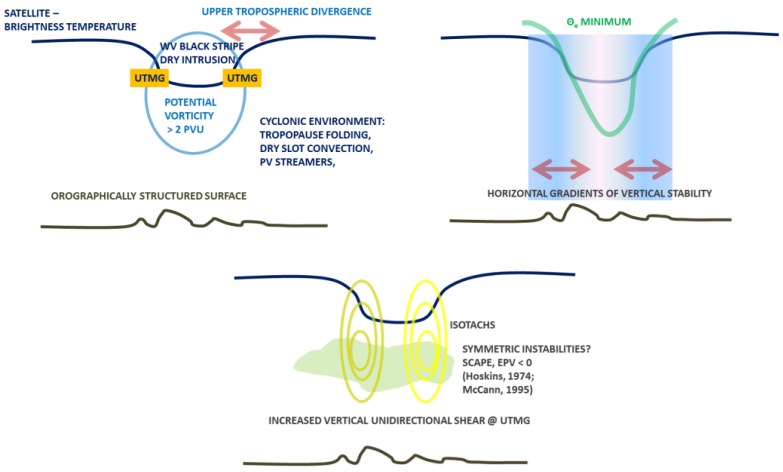

Figure 3.2: Schematic sketch of the dynamic processes related to UTMG (Krennert et al., 2015)

Assuming a synoptic environment as described in section 3.1 with widespread shallow convection over mountainous terrain due to buoyant overturning from elevated surfaces, the question arises of what may contribute to the transition from shallow to deep convection. The impact of moist symmetric instabilities on convection at UTMG represents one of the possible explanations for this transition. The idea is that, assuming an UTMG and the associated dynamical processes as discussed before, a saturated air parcel that is initially prevented from reaching its LFC reaches a zone of negative EPV, which is an indicator for MSI. Due to the release of symmetric instability additional lift is provided and convection develops, possibly according to the concept of the aforementioned *downscale development* introduced by Xu (1986). In combination with horizontal and vertical gradients of equivalent potential temperature and vertical wind shear, a coexistence of both moist gravitational and moist symmetric instability along the UTMG can be expected. This concept, including the related dynamical processes, is sketched schematically in

Fig. 3.2. It is similar to a concept already introduced by Morcrette and Browning (2006). In this study, symmetric instability and ΔM adjustment as mechanisms for slantwise circulations leading to precipitation bands near midlatitude cold fronts have been investigated. ΔM adjustment basically means that, as air parcels are ascending towards their level of neutral buoyancy (LNB), the geostrophic absolute momentum is conserved. Due to atmospheric baroclinicity an absolute momentum anomaly is generated because of different values at the parcel's initial height and their LNB. They emphasized that ΔM adjustment favours the creation of symmetric instability by building regions of negative EPV aloft.

3.4 Atmospheric Lids

Russell et al. (2008) studied the role of atmospheric lids beneath an upper-level PV anomaly and their impact on the initiation of DMC. They defined a *lid* or *capping inversion* as "[...] a stable layer of relatively warm, dry air that has air of higher wet-bulb potential temperature Θ_w beneath it and lower Θ_w above it in the middle and upper troposphere." Beside its role in suppressing convection, the presence of a lid can also promote convection, as it allows for accumulating heat and moisture beneath it and therefore creating conditional instability. In this case sufficient boundary-layer forcing like convergence or orographic lift is needed to overcome the lid and release the instability or otherwise large-scale uplift may contribute to a weakening of the lid (Russell et al., 2008, p. 372).

Graziano and Carlson (1987) defined criteria for the identification of a lid in a sounding. A schematic lid sounding is shown in Fig. 3.3. The lid is characterized by a moist layer and high potential wet-bulb temperature in low levels and a break in relative humidity with a thermal inversion above it (Fawbush and Miller, 1952).

Graziano and Carlson (1987) have shown that convection tends to be more severe in the presence of a lid, although it is more likely to occur in its absence.

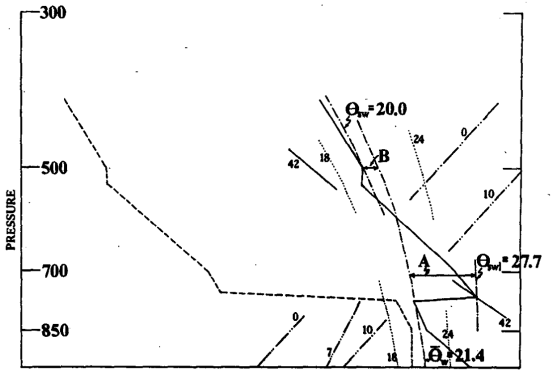

Figure 3.3: Identification of a lid on a skew T - log p diagram (Graziano and Carlson, 1987)

3.5 Diabatic Heating

Another hypothesis relating UTMG and DMC deals with the incoming solar radiation and the corresponding surface heating which shows different responses dependent on the humidity in upper levels. Water vapor is the primary absorber in the near-infrared (Liou, 2002). Consequently the incoming solar radiation is reduced beneath a moist upper level layer. Therefore it can be expected that the surfaces below a dry upper level area are heated to a greater extent than the surfaces below a moist layer (Krennert and Zwatz-Meise, 2003, p. 361).

3.6 The Convective Storm Initiation Project

Linking some of these concepts and features related to UTMG and its impact on convective initiation is done by summarizing the results of a case study in the course of the Convective Storm Initiation Project (CSIP).

CSIP was an international project during the summers of 2004 and 2005 with the aim of understanding why, where and when deep convection breaks out. Therefore, detailed observations of convective clouds were taken and compared to high resolution numerical weather prediction models. The main field campaign was implemented over southern England during summer 2005. Several instruments like Doppler radars, wind profilers, lidars, aircraft were deployed for observations. A 12-km operational mesoscale model and a 4-km nested model were used for forecasting convection, both using the same initial conditions (Browning et al., 2007, p. 1943).

Based on the results of this project Russell et al. (2009) published a study on the influence of a descending dry layer on convection in combination with low-level moist convergence over southern England on 18 July 2005. On that day a narrow line of convective showers formed behind a cold front beneath two dry layers, one of which was associated with a tropopause fold. The aim of the study was to analyse the upper-level forcing, hence the influence of the dry layers on convection.

The time-pressure plot in Fig. 3.4 shows the evolution of the dry layers (represented by the 10% relative humidity isoline) with bases at 650 and 400 hPa, approximately. From the radar data it can be seen that the precipitation started at around 15:45 UTC. A region of high Θ_w indicates the presence of a lid between 14:30 and 15:30 UTC at around 850 hPa. The boundary layer contributed to the development of the convective showers by introducing potential instability and by weakening the lid that had suppressed convection at that time (Russell et al., 2009).

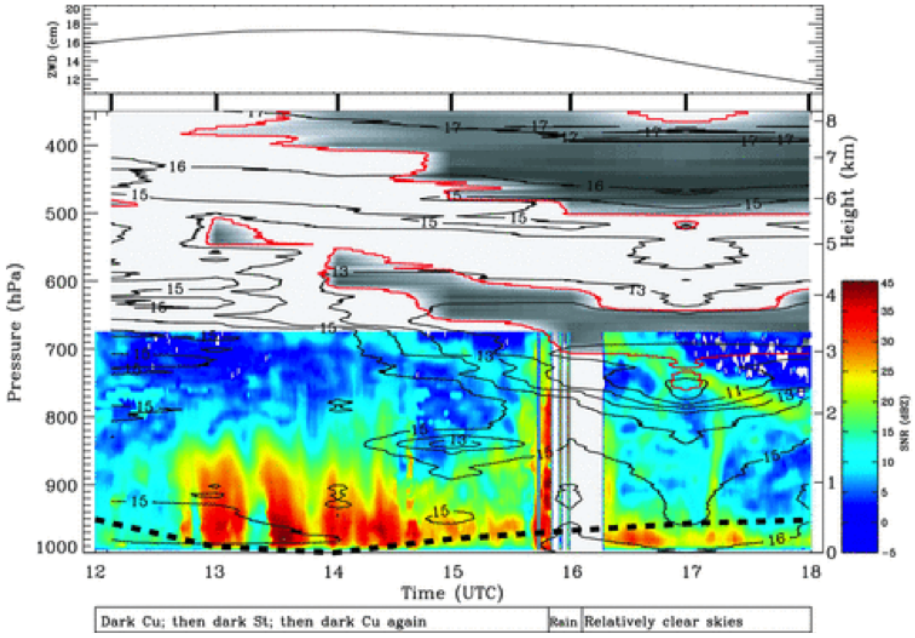

Figure 3.4: Time-pressure cross section of wet-bulb potential temperature (Θ_w, solid lines), the < 10 % relative humidity (RH) area (grey shading), the 10 % RH contours (red lines) and the lifting condensation level (thick black dashed line) from the Swanage soundings for 18 July 2005 (Russell et al., 2009, p. 255)

3.7 Summary

To summarize, the following hypotheses and questions shall be tested based on case studies with WRF:

- Is the model able to resolve DMC and at what horizontal resolution?
- Which of the previously discussed concepts can be related to single-cell convection at UTMG?
- What types of instabilities are involved?

Chapter 4

Case Study - 7 July 2014

In the morning of 7 July 2014, shallow convection was observed all over the Eastern Alpine region. The towering clouds in the satellite imagery could be clearly connected to orography, while the surrounding flat terrain remained cloud-free. From 10:30 UTC distinct deep convective clouds were visible and it appeared that their initiation could be related to an upper-level water vapour gradient in the satellite imagery.

4.1 Synoptic Overview and Observations

The area of interest is the south-eastern part of Lower Austria close to the Styrian border, including the mountainous area of Wechsel. The reanalysis of 500 hPa and surface pressure (Fig. 4.1) indicates a pressure ridge over the eastern part of Austria while a cold front is situated over Western Europe. Fig. 4.2 shows a radio sounding taken in Vienna at 12:00 UTC. The vertical distribution of the relative humidity indicates the dry intrusion and also shows a distinct vertical moisture gradient between 600 and 450 hPa. The level of free convection can be found at approximately 700 hPa.

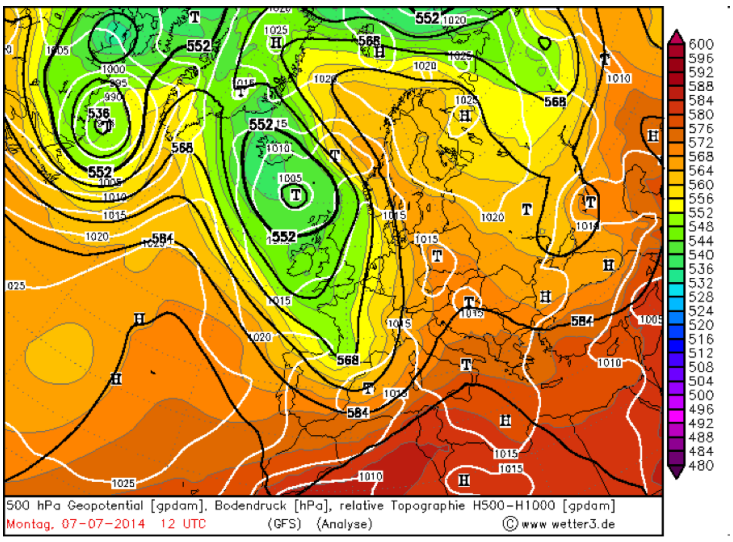

Figure 4.1: GFS analysis at 12:00 UTC showing geopotential height [gpdm] at 500 hPa (thick bold lines), surface pressure [hPa] (white bold lines) and relative topography H500 - H1000 [gpdm] (shading). ©www.wetter3.de

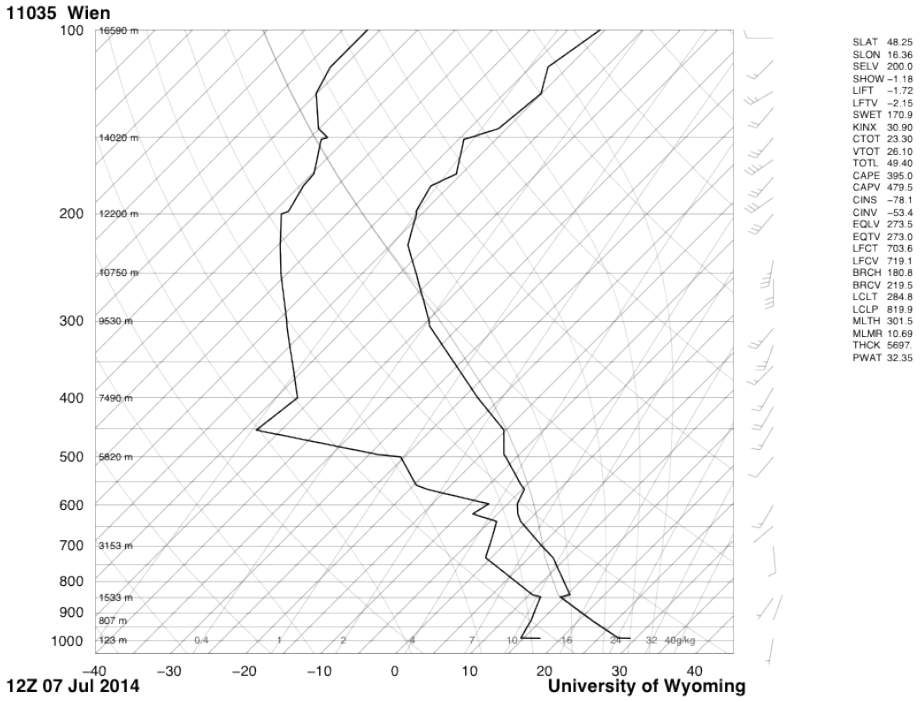

Figure 4.2: Skew-T log-p diagram for Vienna at 12:00 UTC on 7 July 2014 (University of Wyoming, 2016)

Fig. 4.3 shows a series of RGB (red/green/blue) satellite image composites with overlaid radar reflectivity at four different times. The 09:30 UTC satellite imagery indicates shallow convection over the Eastern Alpine region and clearly shows the UTMG, represented by a black stripe in the WV channel which stretches from north-eastern Germany to Bosnia and Herzegovina. At 10:00 UTC the signal in the (IR) 9.7 µm channel within the area of UTMG becomes more pronounced, indicating the growing of shallow convective cells, which is also supported by the radar reflectivity. At 10:30 UTC deep moist convection has developed along one point at the UTMG, as depicted by an enhanced signal in satellite and radar reflectivity data.

These observations are supported by a few ESWD (European Severe Weather Database) reports. The ESWD is a collection of severe weather reports established by the European Severe Storms Laboratory (ESSL) with the aim of providing detailed and high-quality information useful for scientific analysis (Dotzek et al., 2009). Fig. 4.4 shows ESWD reports for 7 July 2014 between 09:00 and 14:00 UTC in Austria. There are two reports of damaging lightning, one report of severe wind and one report of heavy rain in the south-eastern part of Lower Austria and one report of heavy rain in Styria between 11:30 and 13:00 UTC. The information is based on newspaper and eyewitness reports and provides evidence for convective development in the area of interest.

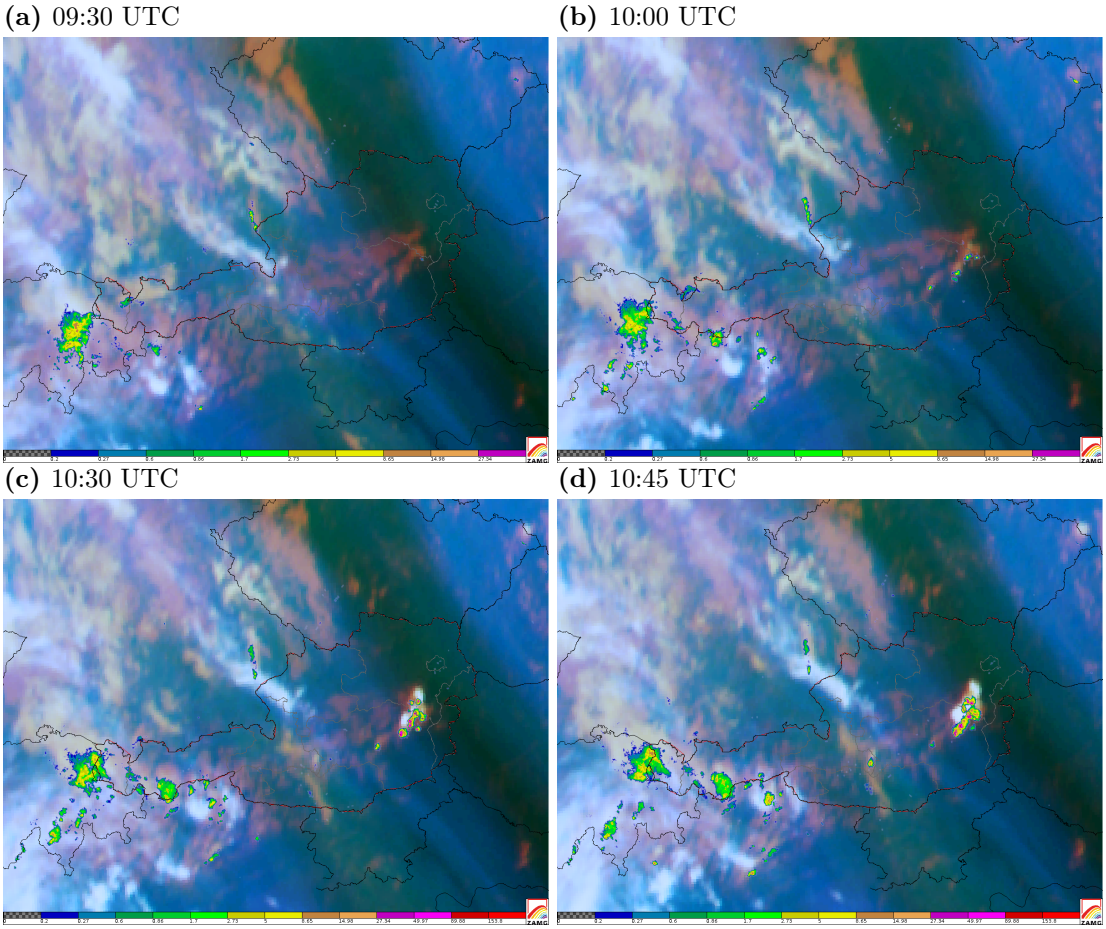

Figure 4.3: MSG (meteosat second generation) RGB (red/green/blue) satellite image composites where low level moisture is represented by the IR 9.7 µm channel (red), mid level moisture by the WV 7.3 µm channel (green) and high level moisture by the WV 6.2 µm channel (blue). Radar reflectivity data in MAXCAPPI (maximum constant altitude plan position indicator) format is overlaid additionally. ©ZAMG

Figure 4.4: ESWD reports from 09:00 UTC - 14:00 UTC on 7 July 2014. Blue circles indicate heavy rain, red flashes indicate damaging lightning and the yellow square marks severe wind (Dotzek et al., 2009).

4.2 Model Configuration

4.2.1 The WRF model

The WRF mesoscale numerical weather prediction model (Version 3.7), with the Advanced Research WRF (ARW) fully compressible and non-hydrostatic dynamical solver, was used for the simulations. The model uses a terrain-following, pressure-based vertical coordinate (eta-coordinate) with a constant pressure surface at the model top and an Arakawa C-grid staggering for the horizontal grid (Skamarock et al., 2008).

4.2.2 Model settings

The initialization time of the simulation had a notable influence on the results and after some sensitivity tests it turned out that initializing the model at 18:00 UTC on 6 July 2014, which is about 16 hours before the initiation of DMC, gave the most adequate results. The simulation was performed with three nested domains (one-way nesting) with horizontal grid spacings of 20 km, 4 km and 0.8 km, respectively, and 61 vertical levels with monotonically increasing thickness. The model top was specified at 25 hPa. The location of the domains was chosen as follows: Domain 1 mainly spans Europe down to the North African coast to capture the dynamical processes related to the upper-level moisture gradient. Domain 2 covers Central Europe and is basically used for comparison with the smallest domain and for testing its performance in resolving convection. Domain 3 covers the eastern Alpine region, including the area where convection broke out. The initial and boundary conditions for the integration were derived from ECMWF (European Centre for Medium-Range Weather Forecasts) analysis data with 6-h temporal resolution. The positions of the computation domains are shown in Fig. 4.5.

For the parameterization of cumulus physics, a Grell 3D Ensemble Scheme was used for Domain 1, while no parameterization was applied to Domains 2 and 3, as they are considered to be convection-resolving. For microphysics, the WSM6 (WRF single moment 6-class) scheme was used, which is an extension of the mixed-phase (WSM5) scheme implemented by Lim and Hong (2005). The WSM6 scheme includes graupel mixing ratio as additional prognostic water substance variable besides mixing ratios of water vapour, cloud water, cloud ice, rain and snow (Hong and Lim, 2006). The Mellor-Yamada-Janjic (MYJ) scheme was applied to boundary layer turbulence. It uses the 2.5 level turbulence model of Mellor and Yamada (1982). Eddy diffusion coefficients are derived from the turbulent kinetic energy (TKE) (Janjić, 2002). The land surface was handled by the Noah land surface model, which is a four-layer temperature and moisture model (Tewari et al., 2004). It provides sensible and latent heat fluxes. Ground heat flux is computed by the thermal diffusion equation (Chen et al., 1996). For shortwave and longwave radiation, the Dudhia Shortwave scheme (Dudhia, 1989) and RRTM Longwave scheme (Mlawer et al., 1997) were applied.

Table 1 gives an overview of the aforementioned physical parameterization options. The

impact on the horizontal resolution is visible by a contour plot of topography for each domain, as shown in Fig. 4.6. While the representation of topography is not very precise for Domain 1, the complex structure of the mountainous terrain is well represented by the two inner domains.

Table 1: WRF parmeterization options

Substance	WRF Scheme
Microphysics	WSM-6 Scheme
Planetary Boundary Layer	Mellor-Yamada-Janic Scheme
Longwave Radiation	RRTM Longwave Scheme
Shortwave Radiation	Simple Shortwave Scheme
Land Surface	Unified Noah Land Surface Model
Surface Layer	Eta Similarity Scheme

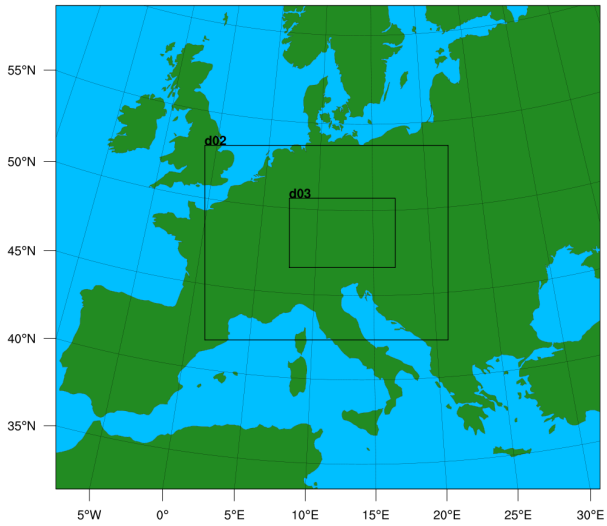

Figure 4.5: Location of domains

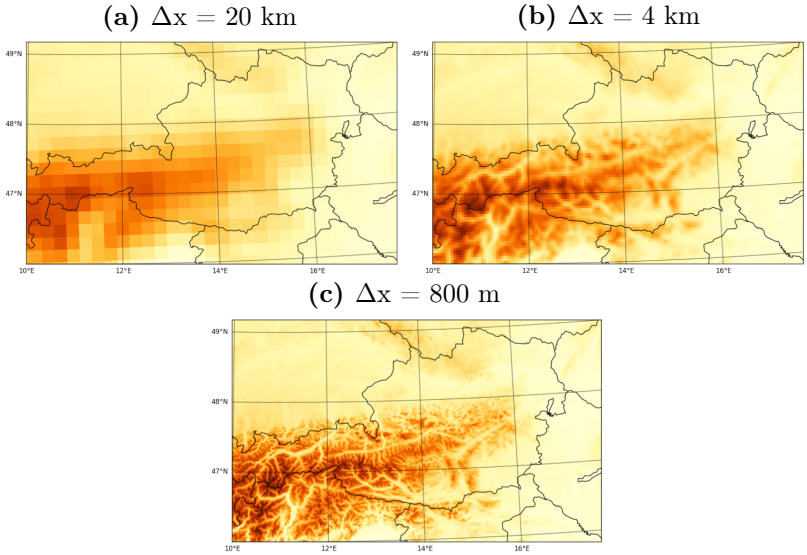

Figure 4.6: Representation of Model Topography for each domain

4.2.3 Post-Processing

The main part of post-processing, i.e. analysing and plotting data, was done using the programming language Python (version 2.7) which provides powerful tools and packages for handling and plotting netcdf data. It was also used for interpolating model level data to levels of constant height or pressure, which makes analysing data easier. A strong tool for drawing 2D WRF output on maps is *basemap* as it allows to transform coordinates to many different map projections. With the tool *matplotlib* contours, images, vectors, lines or points can then be plotted in the transformed coordinates.

4.3 Results

4.3.1 Pre-storm Conditions

The following figures provide an overview about the synoptic pre-storm conditions in Domain 1. The distribution of 500 hPa geopotential height and sea-level pressure at 09:00 UTC clearly show the ridge affecting the Eastern Alpine Region and weak gradients in the pressure surface field (Fig. 4.7).

The distribution of equivalent potential temperature (Fig. 4.8a) shows the approaching front over Western Europe, i.e. Western Germany, and indicates an area of warm, moist airmasses over Eastern Austria, including the area of interest. In general, the synoptic conditions allow for considering a fair-weather situation.

The UTMG, as indicated by the dark blue stripe in the 300 hPa distribution of relative humidity (Fig. 4.8b), is well represented and stretches from Eastern Germany to Bosnia and Herzegovina. It matches the location of the gradient in the water vapour satellite images (Fig. 4.3) reasonably well.

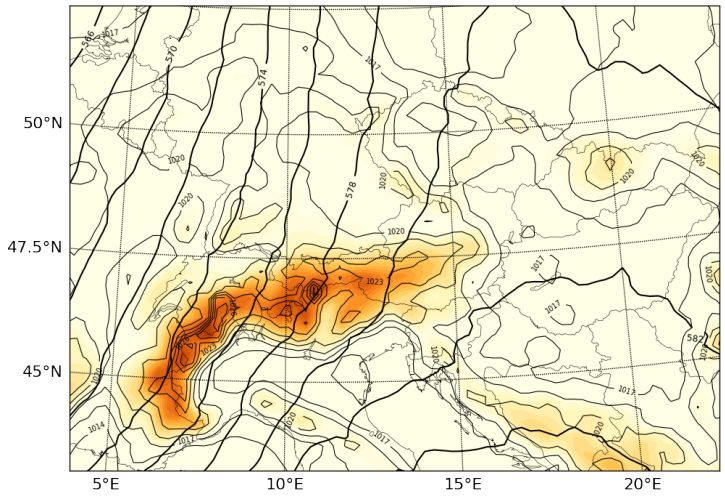

Figure 4.7: 09:00 UTC: Geopotential height [gpdm] at 500 hPa (thick solid lines) with intervals of 2 gdpm and sea-level pressure [hPa] (thin solid lines) with contour spacing of 3 hPa. The terrain is represented by an orange color-shading for levels above 500 m.

Fig. 4.9a presents a vertical west-east cross-section of relative humidity and horizontal wind speed in Domain 1. The UTMG, or dry intrusion, is clearly evident (dark blue zone) and shows distinct vertical and horizontal gradients in relative humidity in the middle and upper troposphere. A second dry intrusion, although weaker, is found at approximately 200 km to the east. The bases of the dry intrusions are found at 5 and 4 km, respectively. There is also a zone of high relative humidity in the lower levels above mountainous terrain. Significant gradients in wind speed are found between 4 and 6 km, indicating vertical wind shear.

A west-east vertical cross-section of EPV and Θ_e (Fig. 4.10a) shows that a zone of negative EPV with values between -1 and -2 PVU can be found between heights of 2 and 3 km straight

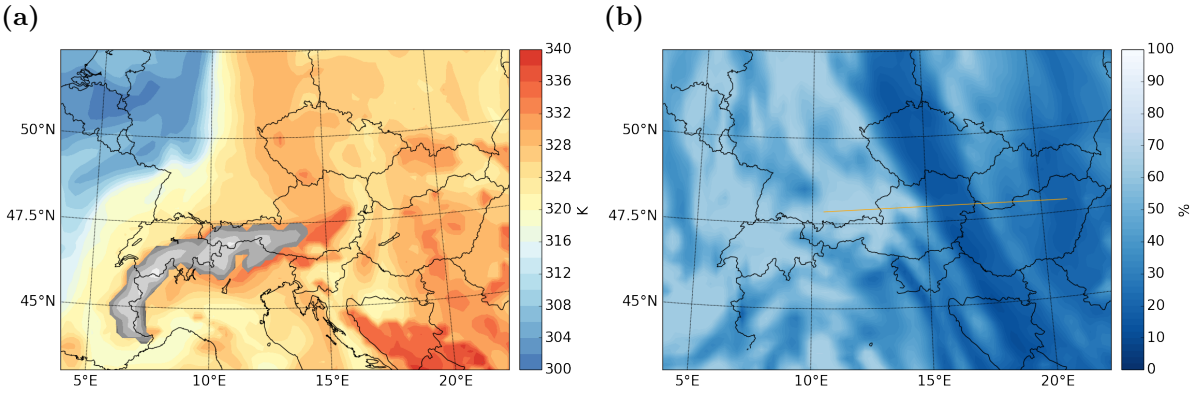

Figure 4.8: Pre-storm conditions in Domain 1 at 09:00 UTC: (a) equivalent potential temperature at 850 hPa; topography is indicated by grey shadings; (b) relative humidity at 300 hPa. The orange line represents the location of the vertical cross-sections in Fig. 4.9 and Fig. 4.10

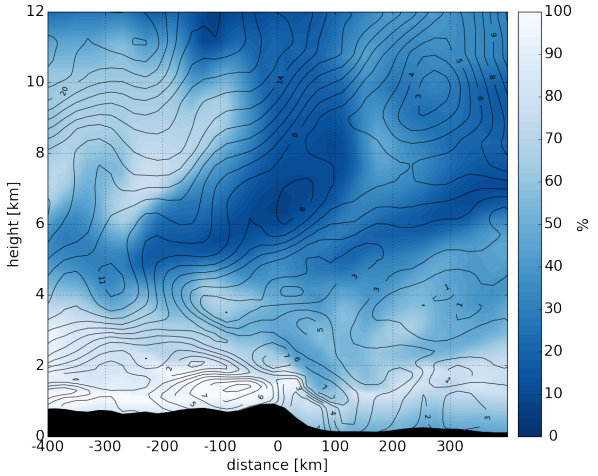

Figure 4.9: West-east vertical cross section in Domain 1 at 09:00 UTC, the location indicated by the orange line in Fig. 4.8b. Relative humidity [%] (shaded) and horizontal wind speed [m/s] (black solid lines, contour spacing: 1 ms^{-1}). The black shading represents topography, as resolved by the model

above the area of interest which is an indicator for *potential* symmetric or gravitational instability. The latter is clearly visible by looking at the vertical distribution of Θ_e. Negative/positive gradients are corresponding to negative/positive EPV. Minima of Θ_e can be found between 4 and 6 km above ground. Positive values of EPV - in the order of 0.5 - 1 PVU - are found within the dry intrusions, which is characteristic for these features (see 3.2). However, there is no evidence of a tropopause fold, i.e. a folding of the dynamical tropopause (corresponding to the 2 PVU contour) back on itself. The distribution of EPVs (Fig. 4.10b) shows significant negative values at the boundary layer in the east which can be related to strong negative gradients in Θ_e^*. Values between -2 and -3 PVU are detected between 2 and 4 km above the area of interest which marks a region susceptible for *conditional* symmetric or gravitational instability, which again is accompanied by a negative gradient in Θ_e^*. It should be mentioned here that EPV and EPVs are calculated by using the full model wind components u and v instead of using the geostrophic

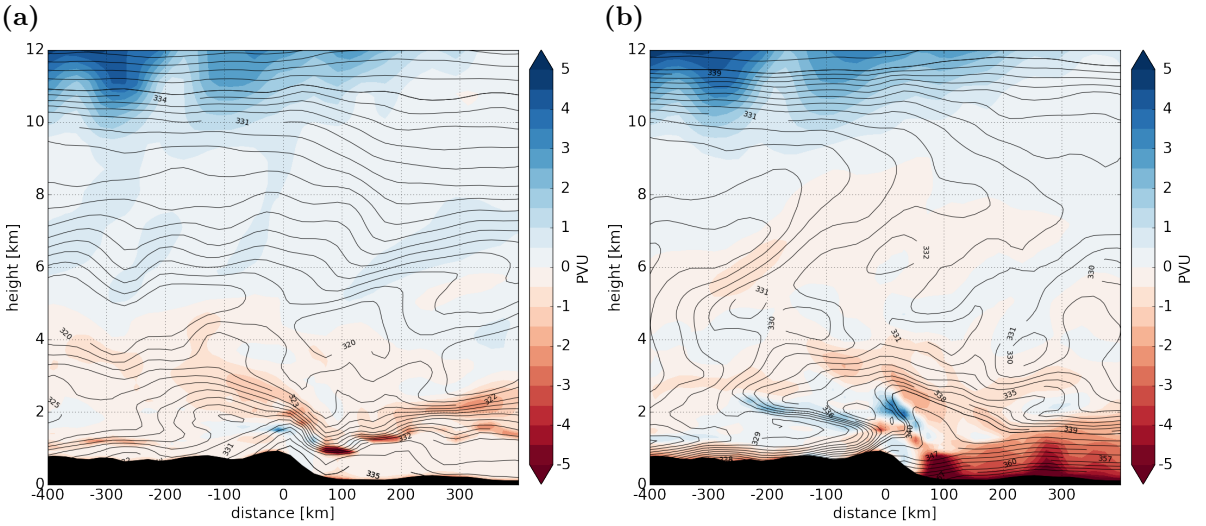

Figure 4.10: West-east vertical cross section in Domain 1 at 09:00 UTC, the location indicated by the orange line in Fig. 4.8. (a) EPV [PVU = 10^{-6}Km^{2}kg^{-1}s^{-1}] (shaded) and equivalent potential temperature [K] (black solid lines), (b) EPVs [PVU] (shaded) and saturated equivalent potential temperature [K] (black solid lines).

wind components u_g and v_g as suggested by McCann (1995). This method is applied during the entire work.

4.3.2 Convective Initiation

What caused the initiation of DMC and how was it related to the UTMG?

In section 4.3.1 the synoptic conditions related to UTMG were discussed, based on output from Domain 1, resulting in the assumption that the environment seems to support the initiation of DMC, in view of the aforementioned characteristics and hypotheses (see Chapter 3). In a next step, the convective initiation is studied in detail and for that reason, results from the convection-resolving domains (2 and 3) are analysed in a period from 06:00 to 10:00 UTC. The following figures represent an analysis of the evolution of the near-surface parameters potential temperature, water vapour mixing ratio and wind as well as the convection-related indices CAPE and CIN. The black rectangle marks the area where model convection was initiated.

Figure 4.11 shows the spatio-temporal evolution of the near-surface potential temperature and near-surface water vapour mixing ratio for the investigated period. At 06:00 UTC the water vapour mixing ratio varies from 9-11 gkg^{-1} in the west to 12-13 gkg^{-1} in the east. By 10:00 UTC the mixing ratio has increased everywhere, including the area of interest, where maxima of 15 gkg^{-1} are achieved. The potential temperature field shows a continuous increase of approximately 2 K within this period.

The evolution of the convection-related indices between 08:00 and 10:00 is illustrated in Fig. 4.12. A region of moderate to high CAPE (500 - 1500 Jkg^{-1}) can be detected within the area of interest and even higher values are found in the south, around 47.5°N. At the same time

the northern part of the whole area is characterized by high CIN values (up to 180 Jkg^{-1}). One hour later, CAPE has increased significantly, indicating high conditional instability, while CIN values have decreased everywhere and are zero in the area of interest. By 10:00 the considered section is characterized by CAPE exceeding 2000 Jkg^{-1} while CIN has decreased to zero almost everywhere.

The analysis of the 10-m wind field for the period 08:00 - 10:00 UTC is shown in Fig. 4.13. The investigated area is affected by low-level westerly winds in the west and north-easterly winds in the east, resulting in a NE-SW oriented convergence line, possibly enhanced by orography. Orographically induced convergence lines are often found in mountainous regions like the Alps. They can support the initiation and development of DMC by providing additional lift for air parcels to reach their LFC. The existence of a convergence line is also confirmed by a ZAMG analysis (not shown) of that day. By 10:00 UTC the convergence zone within the investigated area becomes more pronounced and coincides with the area of high water vapour mixing ratio (Fig. 4.11c) .

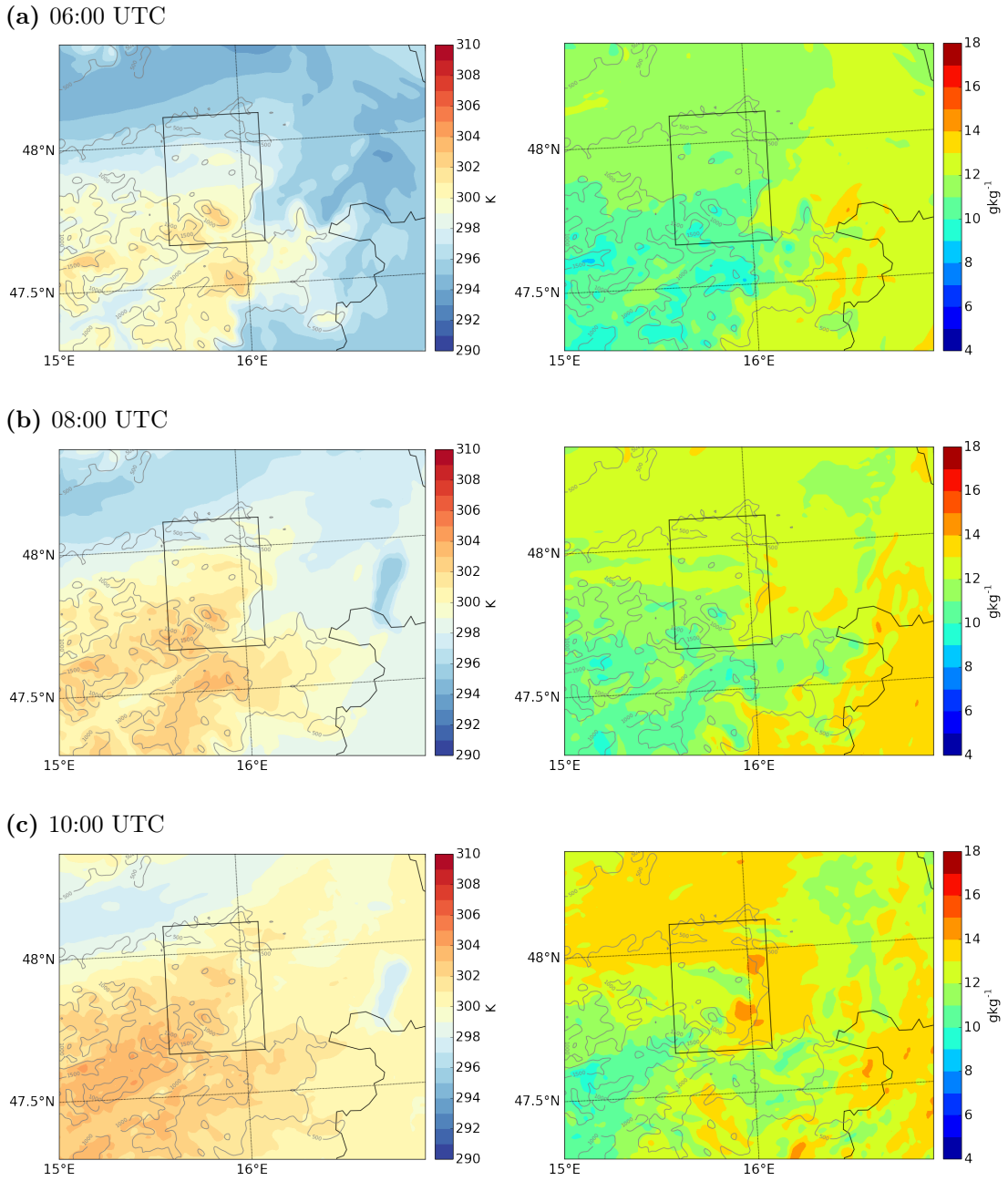

Figure 4.11: Pre-storm conditions in Domain 3. The figure shows the spatio-temporal evolution of near-surface potential temperature (left) and near-surface water vapour mixing ratio (right) at 06:00, 08:00 and 10:00 UTC on 7 July 2014. Grey contours indicate topography (500 m contour spacing)

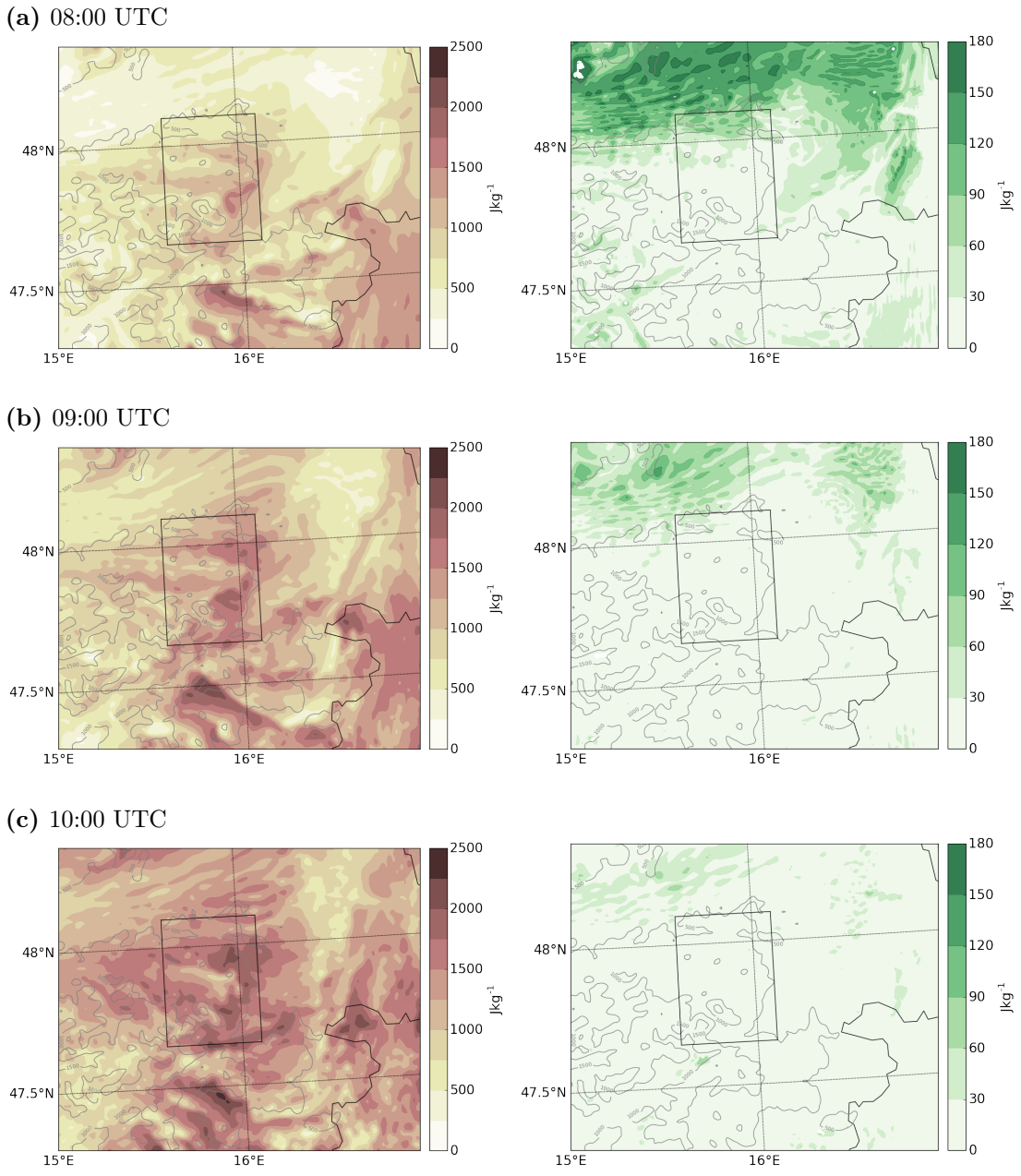

Figure 4.12: Spatio-temporal evolution, 08:00 - 10:00 UTC, of convection-related indices CAPE (left) and CIN (right) on 7 July 2014. Grey contours indicate topography (500 m contour spacing)

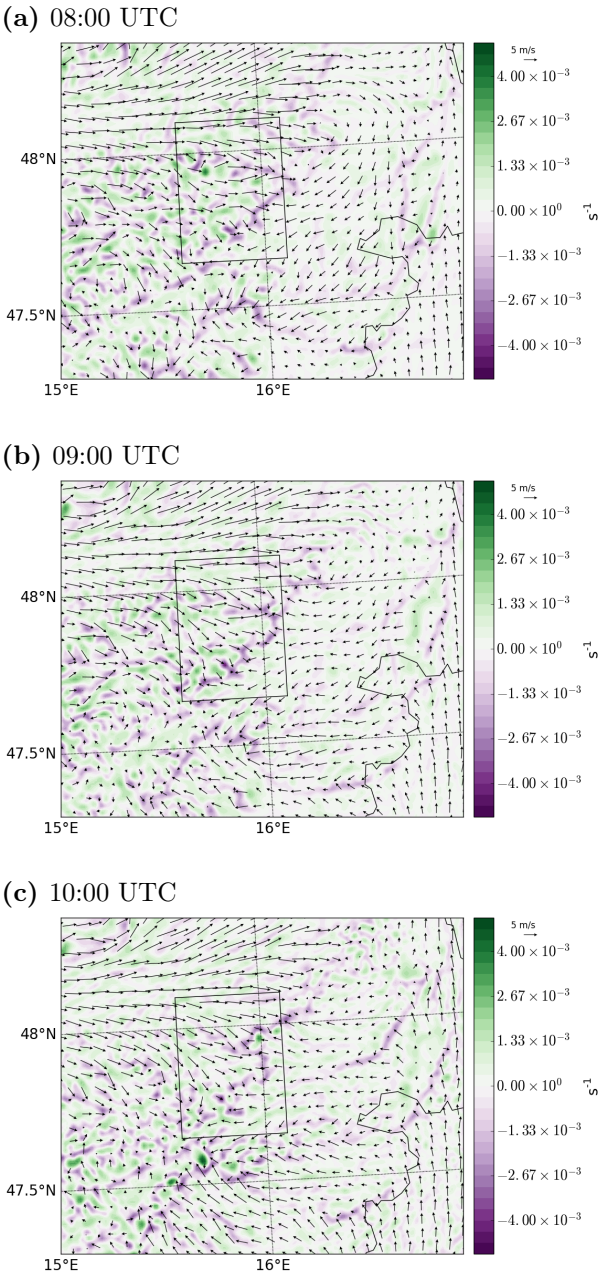

Figure 4.13: 10-m horizontal wind divergence (green = divergence, violet = convergence) and horizontal wind vectors (black arrows) at 08:00, 09:00 and 10:00 UTC

The following figures help investigating the model's ability to resolve convection in Domain 2 and 3. For this purpose, the model's maximum radar reflectivity is analysed between 10:00 and 12:00 UTC (Fig. 4.14).

Generally, the model results show reasonable correspondence with the observations in both timing and location, although they do not match perfectly. Also it appears that there are slight differences depending on the horizontal resolution of the convection-resolving domains.

There is evidence for shallow convection over the Eastern Alpine region in both domains in terms of signals in the radar reflectivity, which is in agreement to the satellite images. At 11:00 UTC the signal becomes more pronounced, indicating growing convective cells. As convection was parameterized in Domain 1 only, it can be concluded that both Domain 2 and Domain 3 resolved the convection adequately even though there is a small lag between the initiation times in both domains. While there is evidence for a full grown DMC in Domain 2 at 10:00 UTC already, distinct DMC emerges about one hour later in Domain 3. Comparing the results to the observed satellite images (Fig. 4.3) yields that the position of the initiation of the modelled DMC can be found more to the east and to the north in both domains, although the shifting is small (in the order of a few tens of km). A more detailed assessment of the model's sensitivity of different microphysic schemes as well as the horizontal domain resolution regarding to convection will be provided in section 4.3.6.

The initiation and development of DMC is also traceable by the 300 hPa relative humidity distribution (Fig. 4.15), where the location of convective initiation, as shown by a clear signal of high values of relative humidity, matches the UTMG, as expected.

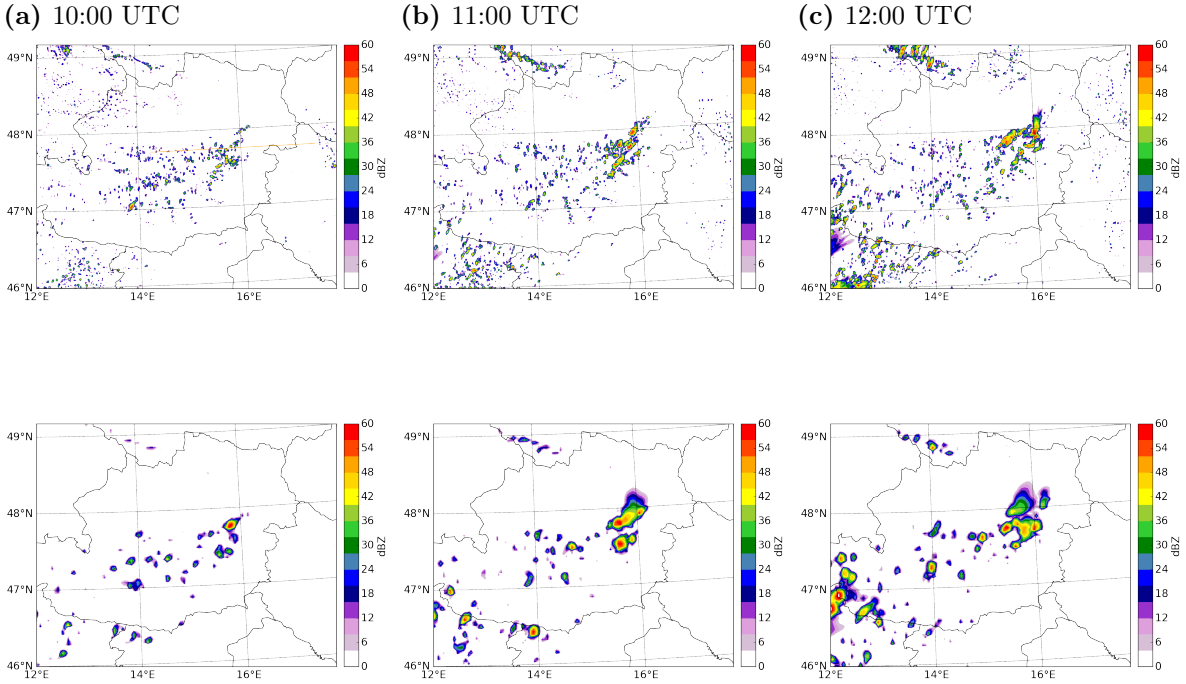

Figure 4.14: Maximum radar reflectivity for Domain 3 (above) and Domain 2 (below) from 10:00 - 12:00 UTC

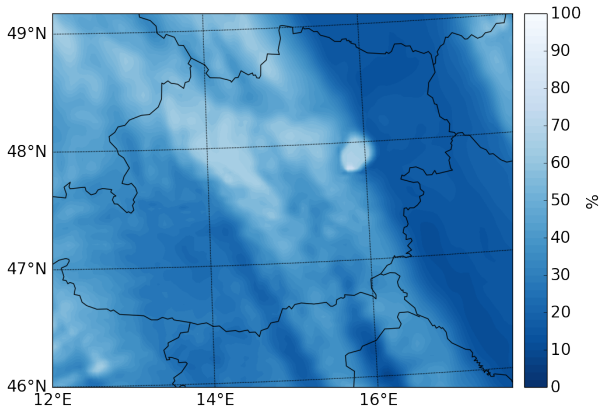

Figure 4.15: Relative humidity at 300 hPa in Domain 2 at 10:30 UTC

4.3.3 Transition from shallow to deep convection

One way to determine simulated moist convection is to take a look at the total hydrometeor mixing ratio $q_{total} = q_r + q_i + q_s + q_c + q_g$ which consists of mixing ratios of rain, ice, snow, cloud and graupel (Kirshbaum, 2011).

The transition from shallow to deep convection can be comprehended by Fig. 4.16 and Fig. 4.17 which show a series of west-east vertical cross-sections of q_{total} with overlaid contours of Θ_e and horizontal wind speed in Domain 3 from 09:00 to 11:00 UTC.

At 09:00 UTC shallow convective towers start to develop over mountainous area - in agreement to the observations - with cloud tops below 4 km. No convective development occurs over flat terrain, i.e. in the right part of the cross-section, which emphasizes the role of orography in triggering convection. Shallow convection is accompanied by a distinct vertical gradient of Θ_e in the area below the UTMG, i.e. between 2 and 4 km above the area of interest. (Fig. 4.16a). One hour later, at 10:00 UTC, the growing of the shallow convective cells towards levels of approximately 4 km can be noticed and additionally, the vertical gradient of Θ_e in lower levels becomes more pronounced. Fig. 4.17b also shows an enhanced vertical wind shear. At 11:00 UTC one of the convective cells has developed into a maturing deep moist convective cloud, reaching levels up to 10 km, accompanied by distinct gradients in horizontal wind speed (Fig. 4.16c and Fig. 4.17c).

Fig. 4.18 displays the vertical profiles of temperature and dew point temperature in a skew-T log-p diagram at 07:00 UTC and 09:00 UTC. At 07:00 UTC a capping inversion can be found with a base at approximately 850 hPa. This lid has been effectively removed by 09:00 UTC, probably due to an increasing temperature in the boundary layer, allowing the further development of shallow convective clouds.

Investigation of the vertical profile of relative humidity in a period from 06:00 to 11:00 UTC (Fig. 4.19) yields a strong vertical gradient with high values in the lower levels and a significant decrease up to 8 km, where the minimum is reached. This corresponds to a typical condition observed in the WV case studies presented by Krennert and Zwatz-Meise (2003). By 08:00 UTC

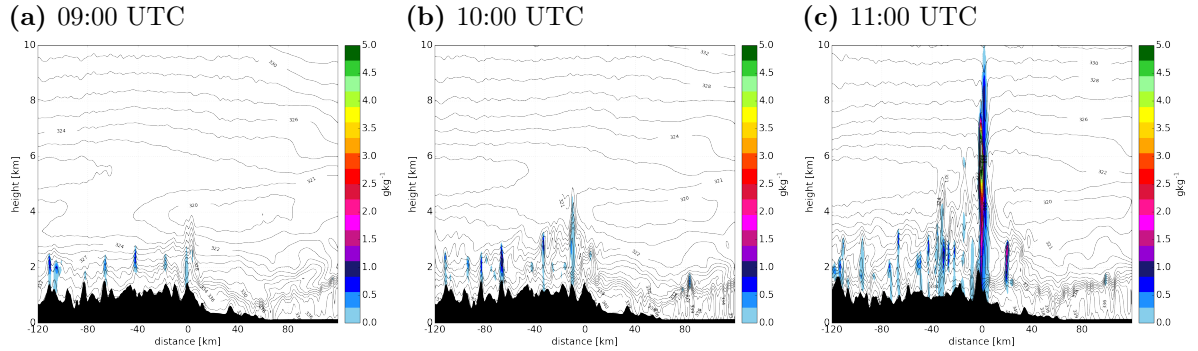

Figure 4.16: West-east vertical cross section of q_{total} (shading) and equivalent potential temperature [K] (black solid lines), 120 km left and right of the considered area, computed from Domain 3. Topography is represented by black shadings.

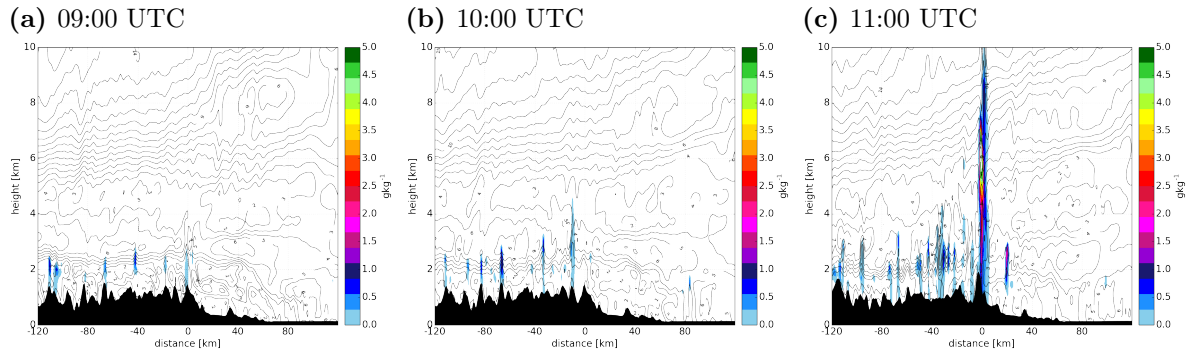

Figure 4.17: West-east vertical cross section of q_{total} (shading) and horizontal wind speed [ms^{-1}] (black solid lines) computed from Domain 3. The location of the cross-section is to be taken from Fig. 4.14a and indicated by an orange line

the relative humidity has increased in lower levels while no significant change can be detected in the upper troposphere. A further increase in low-level humidity and a decrease in the vertical gradient is found at 10:00 UTC. By 11:00 UTC a nearly saturated layer reaches levels up to 9 km, yielding deep moist convective development.

The evolution of potential temperature and water vapour mixing ratio in Domain 2 is investigated between 06:00 and 12:00 UTC, as shown by a Hovmoeller diagram (Fig. 4.20). The PBL water vapour mixing ratio is increasing steadily from initially 10 gkg^{-1} at 06:00 UTC to 12 gkg^{-1} at 09:00 UTC. By 09:00 UTC a mixing ratio of 9 gkg^{-1} is observed up to 2500 m, indicating shallow convective development. The evolution of potential temperature indicates a slight increase of approximately 2 K between 1000 and 1200 m and a slight decrease between 1500 and 2000 m at the same time.

Fig. 4.21 shows the evolution of relative humidity in a time-height cross-section. The dry layer is clearly visible from 04:00 UTC and seems to descend slightly in time. From 08:00 UTC a distinct increase in low-level relative humidity is visible, accompanied by an increased vertical wind shear and finally resulting in the transition to deep moist convection.

(a) 07:00 UTC **(b)** 09:00 UTC

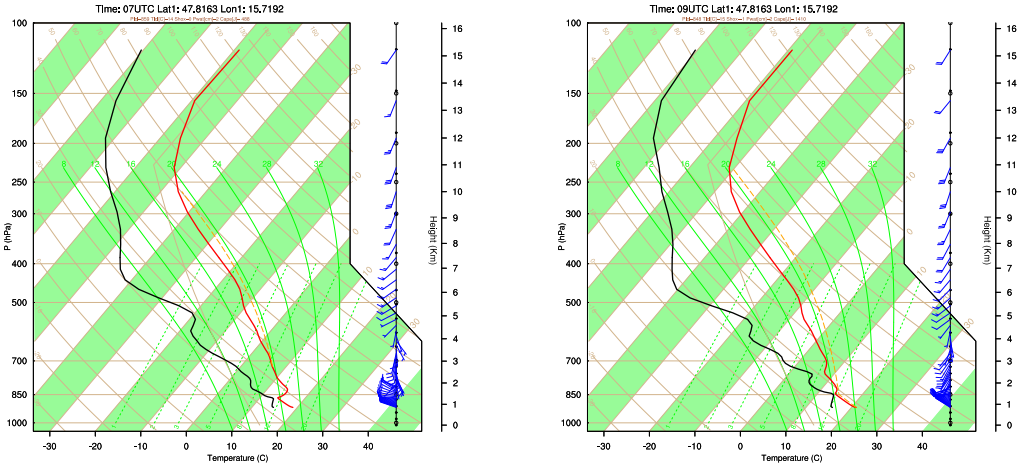

Figure 4.18: Skew-T log-p diagram at 07:00 and 09:00 UTC

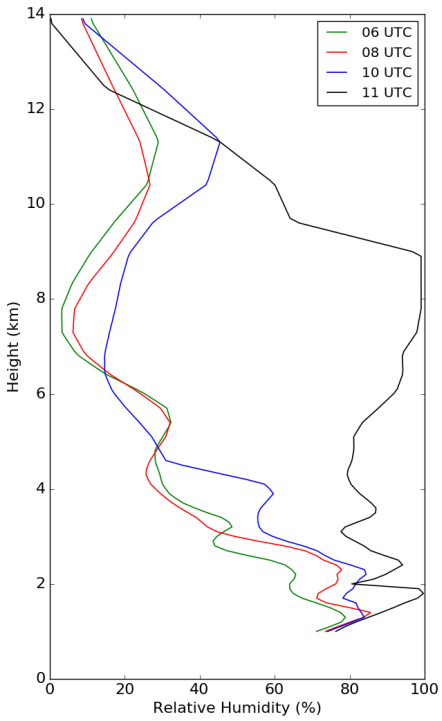

Figure 4.19: Evolution of the vertical distribution of relative humidity [%] at 06:00, 08:00, 10:00 and 11:00 UTC

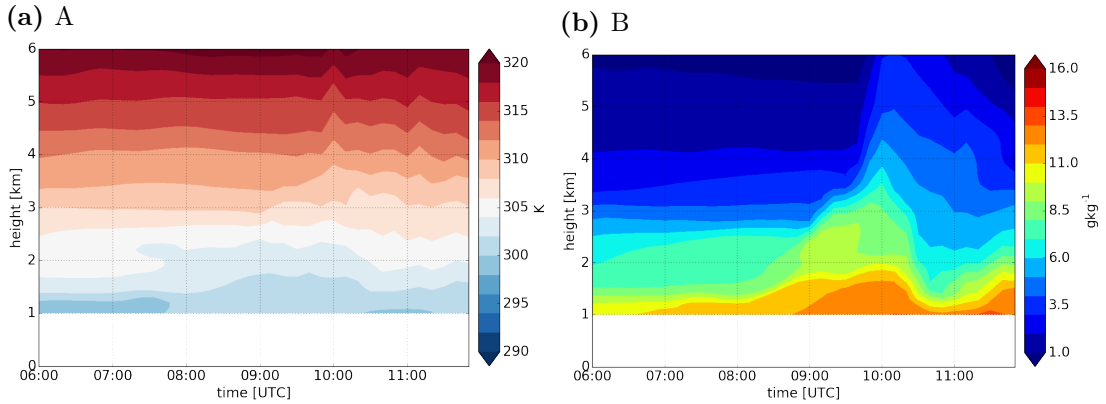

Figure 4.20: Time-height cross-section of potential temperature (left) and water vapour mixing ratio (right) at the location where convection was initiated

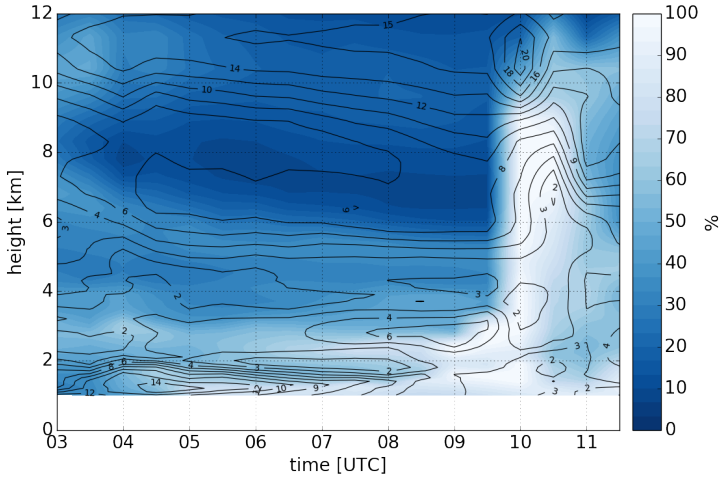

Figure 4.21: Evolution of deep moist convection in Domain 2: time-height cross-section of relative humidity and horizontal wind speed [ms^{-1}] at the location where convection was initiated

4.3.4 Indicators for MSI

In the theoretical part of the thesis two relevant parameters for diagnosing MSI have been introduced: SCAPE and EPV. In the present work, SCAPE was calculated from model output by using a Fortran program, which strongly follows the method introduced by Dixon (1999) (see section 2.1.5). Geostrophic wind components were replaced by the full wind components in the calculation. SCAPE is integrated between levels of 950 and 200 hPa.

Fig. 4.22 shows the horizontal distribution of SCAPE at 09:00 UTC and 10:00, respectively, indicating significant high values, exceeding 3000 Jkg^{-1} within the area of interest. Compared to the horizontal distribution of CAPE (see Fig. 4.12) SCAPE values are much higher.

The horizontal distribution of EPV/EPVs (minima between 750 and 600 hPa) indicates slightly negative EPV values (-1 to -2 PVU) between 14°E and 16°E (Fig. 4.23a) and a region of negative EPVs somewhat more to the East along 16°E (Fig. 4.23b), both of them making this area susceptible to moist (gravitational and symmetric) instabilities. Values were computed from Domain 1 because results from the two innermost domains were too noisy, caused by the gradients of the wind components. The evolution of the vertical distribution of EPV (Fig. 4.24a) at the location of interest shows a significant decrease of EPV down to -3 PVU from 08:00 UTC between 2 and 3 km. Additionally, EPVs is decreasing from 08:00 UTC to even lower values (Fig. 4.24)b. It appears that this favours the transition from shallow to deep convection.

The ingredients of moist gravitational instabilities and moist symmetric instabilities - in terms of gradients in equivalent potential temperature and wind speed, negative values of EPV and high values of SCAPE - seem to be present at lower levels of the troposphere and thus allow for the assumption of a coexistence of both instabilities within this layer. A distinction between these instabilities remains subject of further investigation and will be discussed within the context of the analysis of parcel trajectories (see section 4.3.6).

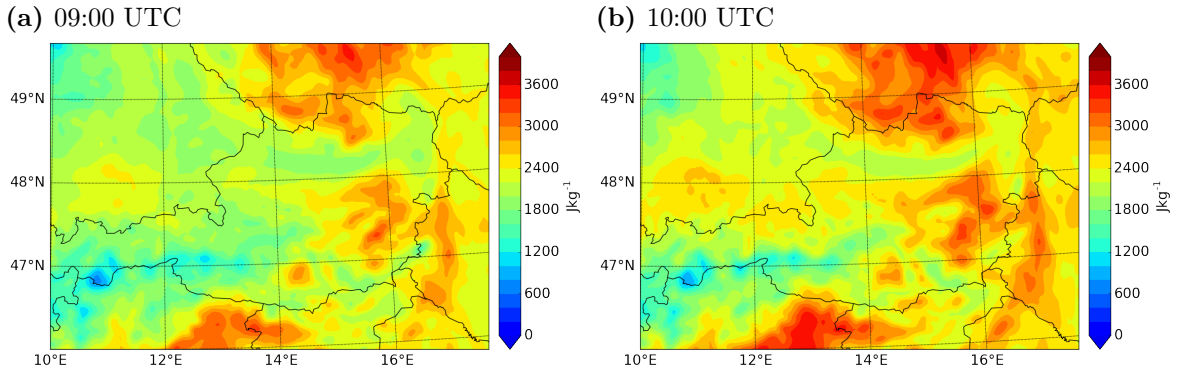

Figure 4.22: SCAPE in Domain 2, 09:00 UTC (left) and 10:00 UTC (right)

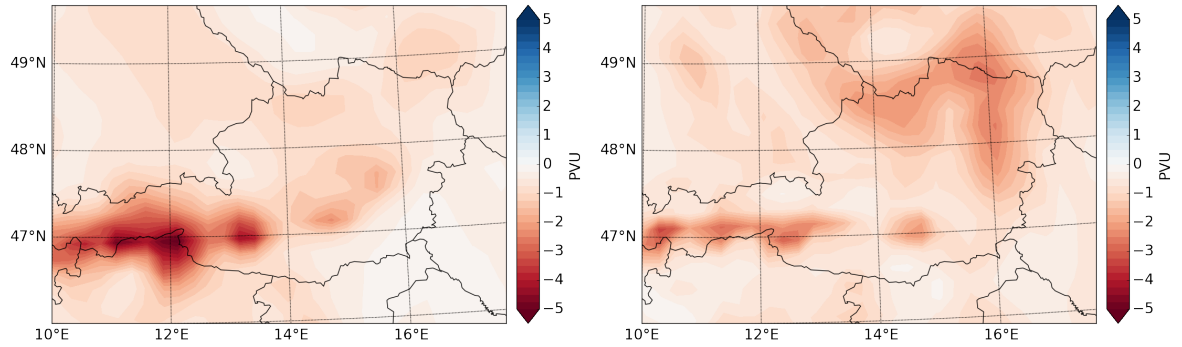

Figure 4.23: Distribution of minimum EPV (left) end EPVs (right) between 750 and 600 hPa in Domain 1 at 10:00 UTC (left)

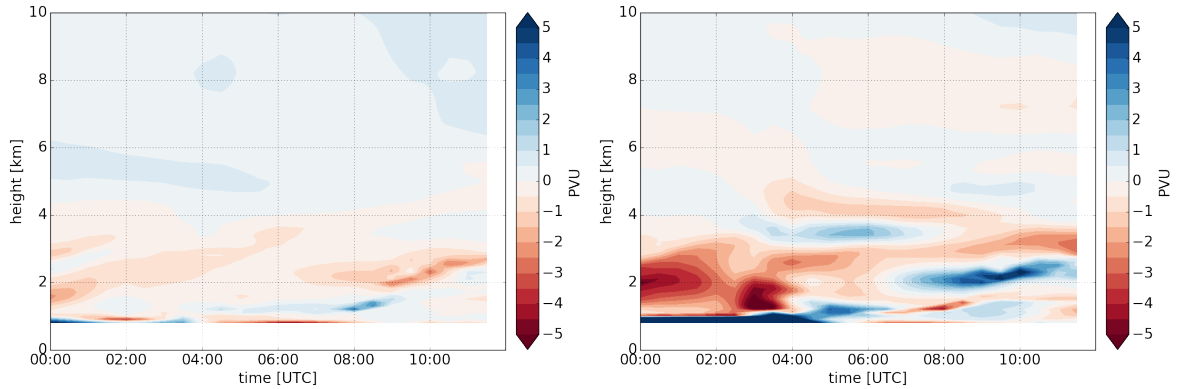

Figure 4.24: Time-height cross-section of EPV (left) and EPVs (right) in Domain 1 at the location where convection was initiated

4.3.5 Sensitivity Tests

In order to test the effect of parameterizations on cloud processes and hence on the storm development, three different microphysics schemes are compared and their performance in modelling deep moist convection is tested. The WSM6 scheme has already been introduced and is used as a reference scheme.

The Thompson scheme (Thompson et al., 2008) is, such as the WSM6 scheme, a single-moment scheme (except for cloud ice and rain) with six prognostic water substance variables, including water vapour, cloud water, rain, ice, snow and graupel. Additionally, the concentration number of cloud ice and rain is predicted. Each hydrometeor species follows a gamma distribution (Thompson et al., 2008, p. 5097).

The Milbrandt-Yau scheme (Milbrandt and Yau, 2005) is a double-moment scheme with seven prognostic water substance variables, including hail as an additional prognostic variable. The concentration number is predicted for each hydrometeor species. The size distributions for each species are described by a gamma distribution function with a spectral shape parameter that is allowed to vary (Milbrandt and Yau, 2005, p. 3055).

Scheme	Reference	Variables
WSM6	Hong and Lim 2006	q_c, q_r, q_i, q_s, q_g
Thompson	Thompson et al. 2008	q_c, q_r, q_i, q_s, q_g
Milbrandt-Yau	Milbrandt and Yau 2005	$q_c, q_r, q_i, q_s, q_g, q_h$

Table 2: Three WRF microphysics schemes and their mass mixing ratios; c,r,i,s,g stand for cloud, rain, ice, snow and graupel, respectively

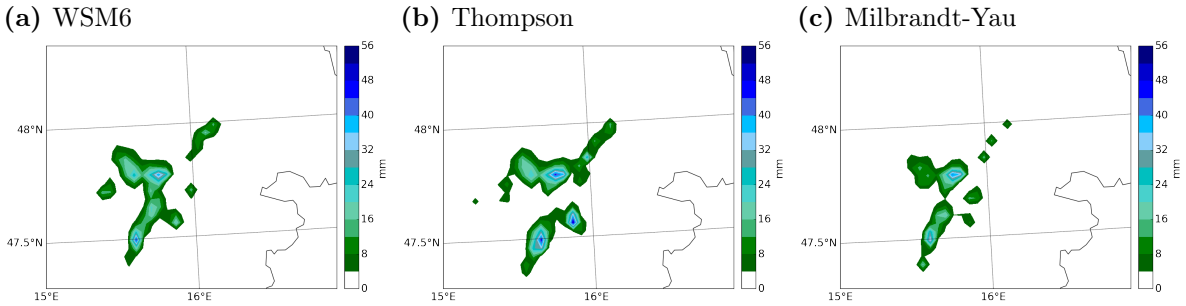

Figure 4.25: 18-h accumulated model rainfall [mm] in Domain 2 for (a) WSM6, (b) Thompson and (c) Milbrandt-Yau parameterization schemes

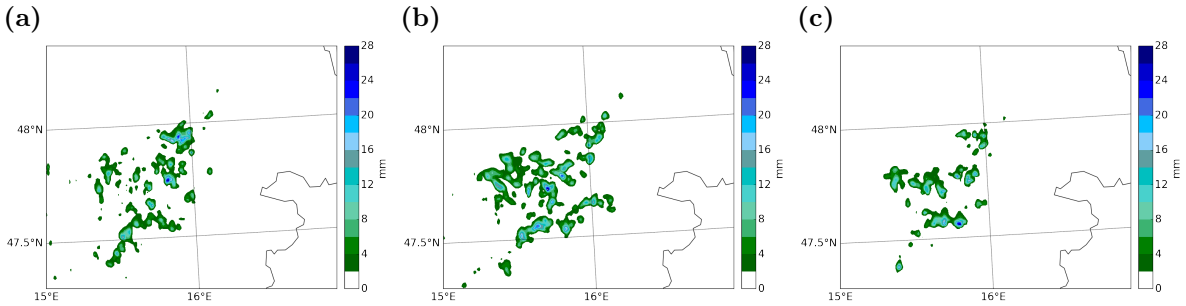

Figure 4.26: 18-h accumulated model rainfall [mm] in Domain 3 at 12:00 UTC for (a) WSM6, (b) Thompson and (c) Milbrandt-Yau parameterization schemes

Scheme	Domain 2	Domain 3
WSM6	44.32	26.66
Thompson	49.91	33.82
Milbrandt-Yau	40.86	27.66

Table 3: 18-h maximum accumulated model rainfall [mm] for three microphysics schemes

An analysis of the 18-h accumulated model rainfall at 12:00 UTC in the area of interest shows slight differences for the considered microphysics schemes, both in Domain 2 and Domain 3 (Fig. 4.25, Fig. 4.26). Considering the 4 km domain, the Thompson scheme covers the greatest area of precipitation and the maximum model rainfall is achieved by this scheme (Table 3), followed by WSM6. Finally, the Milbrandt-Yau scheme produces the smallest accumulated rain rate. Similar characteristics can be found for Domain 3. A comparison of the lower-resolution domain with the high-resolution domain shows that the amount of precipitation is less in Domain

3 for all considered micropyhsics schemes.

Fig. 4.27 shows the maximum radar reflectivity for Domain 2 at 11:00 and 12:00 UTC for the considered microphysics schemes. At 11:00 UTC all schemes show two separate convective cells, more or less at the same location and similar in their structure. The highest reflectivity values (up to 55 dBz) are produced by WSM6 while the lowest values are produced by the Thompson scheme.

The structure of the convective cells becomes more complex for Domain 3 (Fig. 4.28). Greater discrepancies appear between the different microphysics schemes in the structure and intensity of the cells. While the cells produced by WSM6 and the Thompson scheme are smaller and more isolated, the Milbrandt-Yau scheme shows more continuous and larger cells, although their horizontal extent is restricted to a smaller area. Reflectivity maxima of more than 50 dBz are found in all three microphysics schemes. At 12:00 UTC, large and continuous convective cells have developed also in the Thompson and WSM6 scheme. Compared to the Domain 2, the most intense cells develop more northerly for all three microphysics schemes and their horizontal extent is smaller.

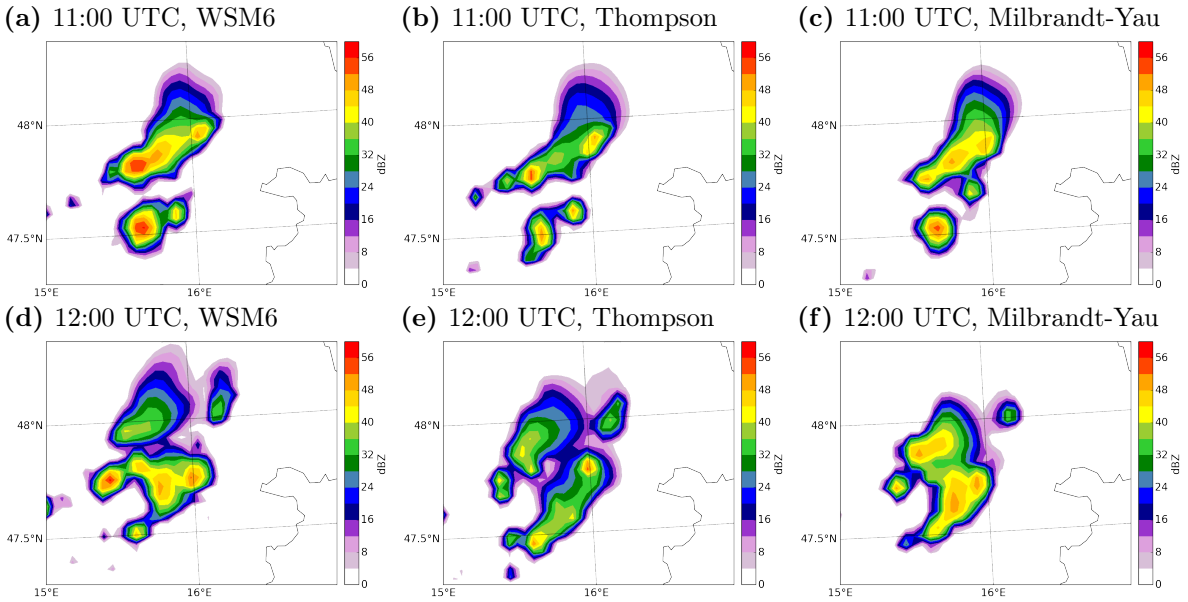

Figure 4.27: Maximum radar reflectivity at 11:00 UTC (a-c) and 12:00 UTC (d-f) for WSM6 (a,d), Thompson (b,d) and Milbrandt-Yau (c,f) parameterization schemes in Domain 2

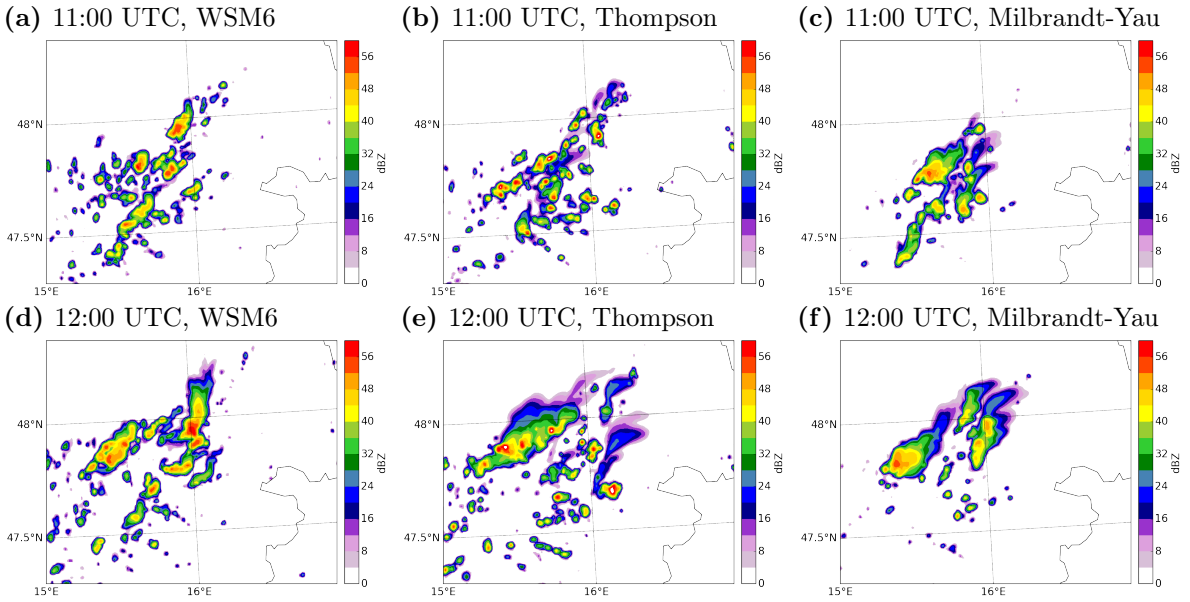

Figure 4.28: Maximum radar reflectivity at 11:00 UTC (a-c) and 12:00 UTC (d-f) for WSM6 (a,d), Thompson (b,d) and Milbrandt-Yau (c,f) parameterization schemes in Domain 3

4.3.6 Parcel Trajectory Analysis

A useful method for analysing the initiation and evolution of convection is provided by the computation of parcel trajectories. Firstly, they might contribute to a better understanding about the processes that lead to the transition of shallow to deep convection, secondly, analysing parcel trajectories might help to distinguish between types of instabilities in terms of predominant wind components and their corresponding accelerations.

The computation of trajectories follows the method described by Stohl (1998), starting with the differential trajectory equation:

$$\frac{d\mathbf{X}}{dt} = \dot{\mathbf{X}}[\mathbf{X}(t)] \tag{4.1}$$

where $\mathbf{X}$ is the position vector, $\dot{\mathbf{X}}$ the wind velocity vector and t time. If the initial position $\mathbf{X}_0$ of a parcel is known, the path or trajectory is fully described by the above equation.

Eq. 4.1 can be solved by expanding $\mathbf{X}$(t) into a Taylor series about $t = t_0$:

$$\mathbf{X}(t_1) = \mathbf{X}(t_0) + (\Delta t)\frac{d\mathbf{X}}{dt}\bigg|_{t_0} + \frac{1}{2}(\Delta t)^2\frac{d^2\mathbf{X}}{dt^2}\bigg|_{t_0} + ... \tag{4.2}$$

The computationally cheapest solution to Eq. 4.2 is the so-called *zero-acceleration solution*:

$$\mathbf{X}(t_1) \approx \mathbf{X}(t_0) + (\Delta t)\dot{\mathbf{X}}(t_0) \tag{4.3}$$

This solution is accurate to the first order as second- and higher-order terms are neglected. There are more accurate approximations like *constant acceleration method* or *variable acceleration method* available but they are computationally expensive.

For the computation of trajectories in the present work, the zero-acceleration method is used as it provides a rather good approximation for short integration time steps. For applying the concept of trajectories to convective cells it is useful to compute backward trajectories which simply means to change the sign in Eq. 4.3.

For analysing the transition from shallow to deep moist convection, back- and forward trajectories were calculated. The initial positions for the forward trajectories have been determined such that they were found within the shallow convective towers. For comparison, eight trajectories were calculated at four different height levels, namely 2000, 2500, 3000 and 3500 m above ground. Fig. 4.29 shows an example for eight 45-min forward trajectories initiated at 2000 m above ground. It can be seen that three trajectories represent the convective updraught reasonably well. One of the three trajectories is chosen for further analysis. The wind components along trajectory 2 (red) are computed and presented as time series where each wind component is represented by a different color. The convective development can be traced by the behaviour of the wind speed and accelerations. The vertical wind component w strongly increases in the first 20 minutes, while at the same time no distinct change can be detected in the horizontal wind

components u and v. The vertical component seems to dominate within this period, indicating upright convection. After approximately 25 minutes, the vertical wind component decreases and the horizontal wind components increase, which can be explained by the fact that the convective tower has reached the tropopause, preventing further vertical extension. An investigation of more trajectories, also at different heights, gave similar results.

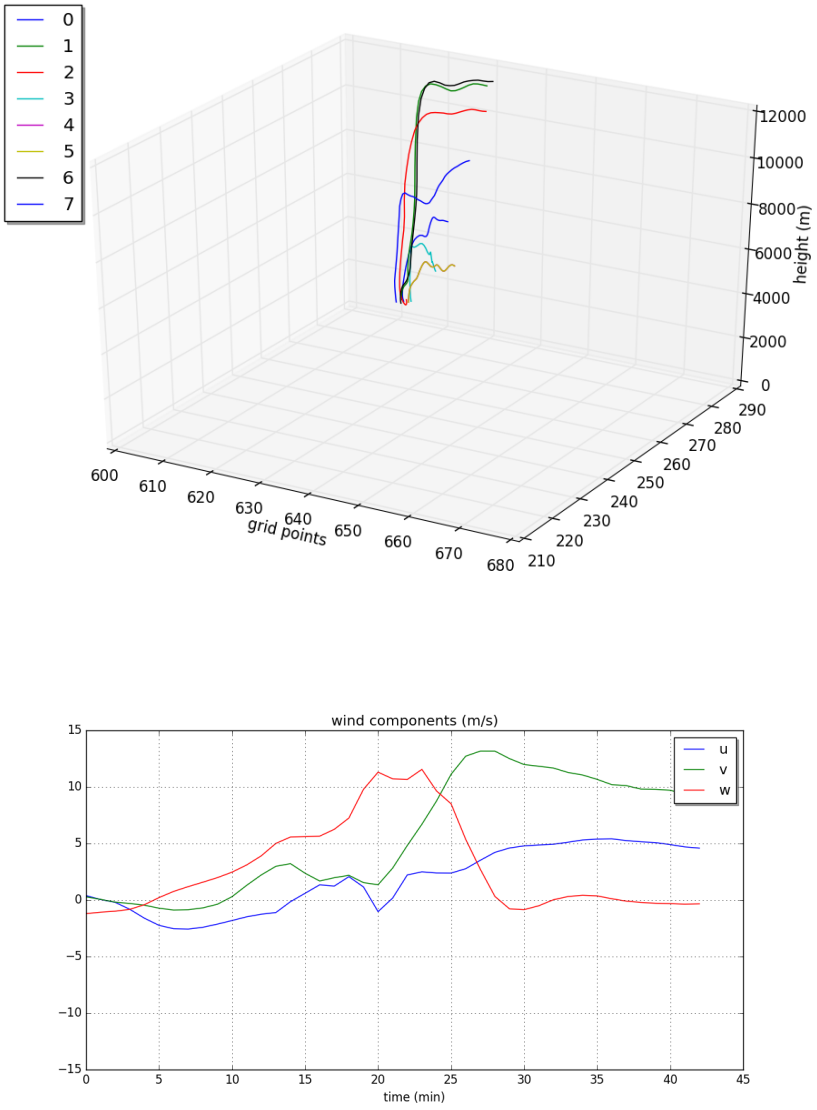

Figure 4.29: 45 minutes forward trajectories (above) and wind components u,v,w along trajectory 2 (below)

Chapter 5

Case Study - 21 July 2013

A second case study dealing with convection related to UTMG will be discussed and analysed, although without going into extensive detail. On 21 July 2013, a gradient in water vapour in midtropospheric levels was observed in the satellite imagery over Northern Italy, close to the Austrian border. In the morning shallow convection was present all over the Alpine region. Deep convective cells started to develop at around 11:00 UTC, where their first initiation could be related to the water vapour gradient in the satellite imagery.

5.1 Synoptic Overview and Observations

The area of interest includes the Alpine region over Northern Italy, south-western Austria and parts of Switzerland. Based on the 500 hPa GFS reanalysis it is shown that central Europe is situated within a pressure ridge (Fig. 5.1).

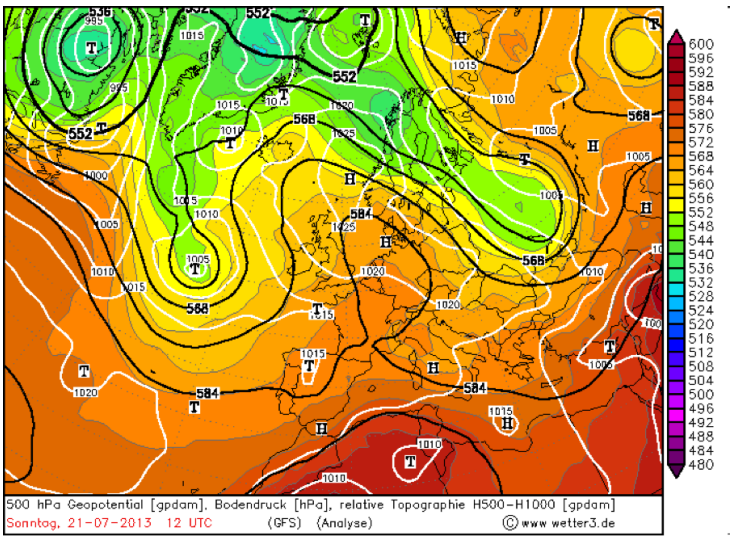

Figure 5.1: GFS (Global Forecast System) analysis at 12:00 UTC showing geopotential height [gpdm] at 500 hPa (thick bold lines), surface pressure [hPa] (white bold lines) and relative topography H500 - H1000 [gpdm] (shading). ©www.wetter3.de

A series of RGB satellite image composites is presented in Fig. 5.2. A dark stripe in the water vapour channel stretches from western Germany down to Northern Italy. At 10:00 UTC shallow convection is present over the mountainous area. At around 11:30 UTC, the first initiation in relation to the water vapour gradient can be noticed over Northern Italy. 30 minutes later, more

deep convective development is visible around the UTMG over eastern parts of Switzerland, westernmost parts of Austria and Northern Italy.

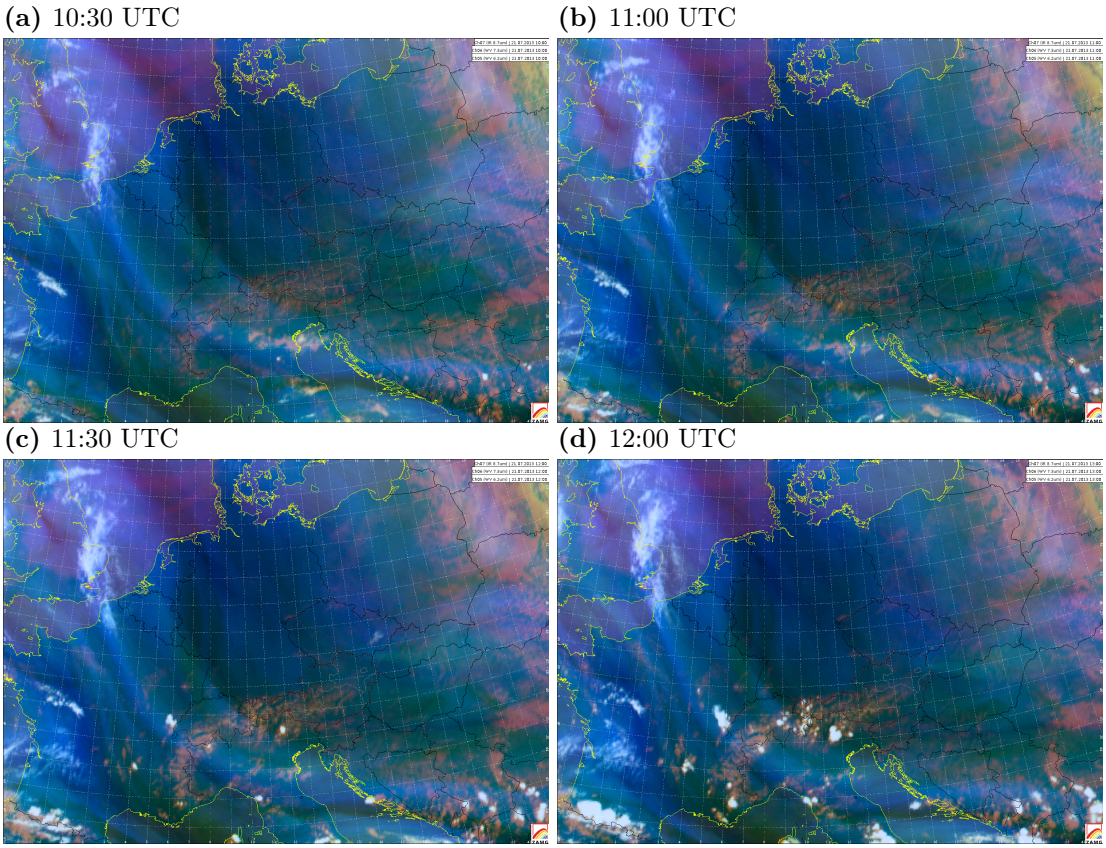

Figure 5.2: MSG (meteosat second generation) RGB (red/green/blue) satellite image composits where low level moisture is represented by the infrared (IR) 9.7 µm channel (red), mid level moisture by the WV 7.3 µm channel (green) and high level moisture by the WV 6.2 µm channel (blue). ©ZAMG

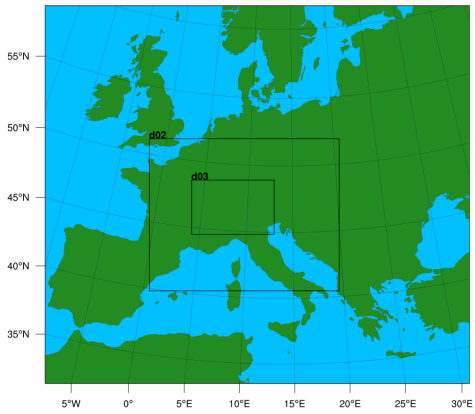

Figure 5.3: Location of domains

5.2 Results

The model setup is equivalent to the previous case study. The positions of the three considered domains are shown in Fig. 5.3. The position of Domain 1 remains the same as in case study 1, while Domain 2 and Domain 3 are shifted to the west so that they cover the area of interest. The simulation was initialized on July 21st 2013 at 00:00 UTC and integrated over 24 hours.

5.2.1 Pre-storm conditions

Large parts of Europe including the Alpine region are dominated by a pressure ridge and weak gradients in the surface pressure field (Fig. 5.4). Warm, moist airmasses in terms of high equivalent potential temperature are dominating the Alpine region (Fig. 5.5a), while no fronts can be detected all over central Europe. The UTMG is clearly visible in the horizontal distribution of relative humidity on the 400 hPa surface (Fig. 5.5b). The dark blue stripe matches the position of the dark stripe in the water vapour channel well. Generally, the synoptic environment can be referred to as a fair weather situation.

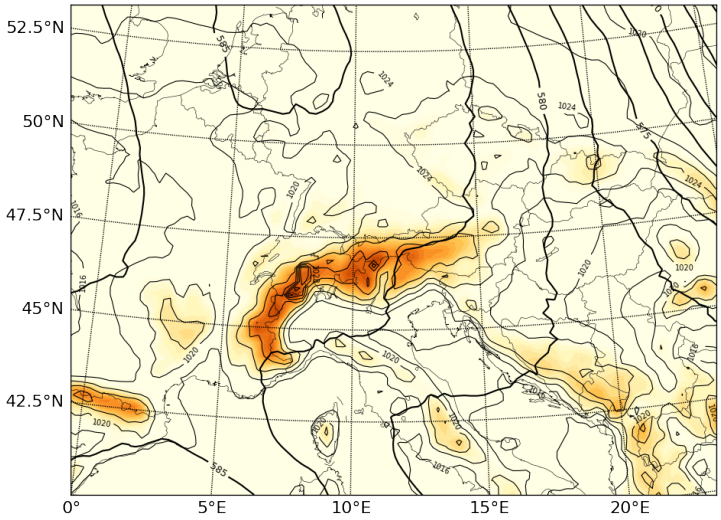

Figure 5.4: 09:00 UTC: Geopotential height [gpdm] at 500 hPa (thick solid lines) with intervals of 2 gdpm and sea-level pressure [hPa] (thin solid lines) with contour spacing of 3 hPa. The terrain is represented by an orange color-shading for levels above 500 m.

A west-east vertical cross-section of relative humidity and horizontal wind speed (Fig. 5.6) displays the vertical distribution of the dry zone. The base of the dry layer can be found at 6 km, approximately. Generally, the vertical extension of the dry layer, as well as the horizontal and vertical gradients in relative humidity are weaker compared to the previous case study. Between 4 and 6 km a vertical gradient in wind speed is found close to the boundary of the dry intrusion.

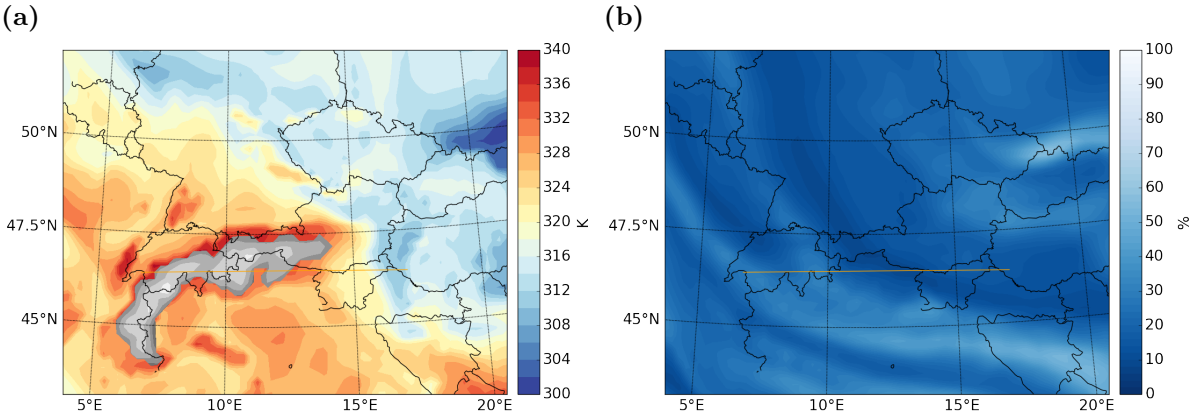

Figure 5.5: Pre-storm conditions in Domain 1 at 10:00 UTC: (a) equivalent potential temperature at 850 hPa; topography is indicated by grey shadings; (b) relative humidity at 400 hPa.

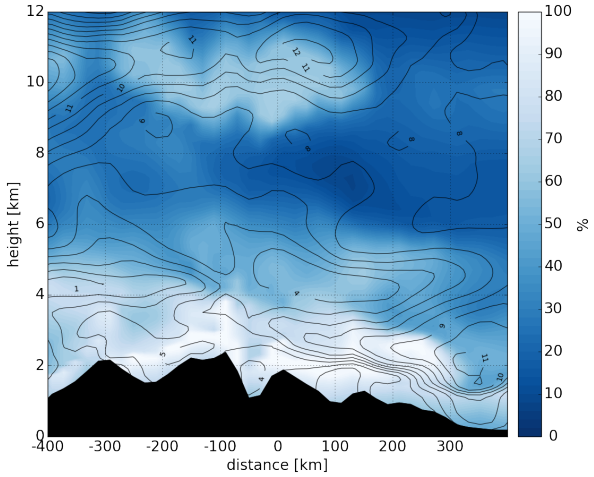

Figure 5.6: West-east vertical cross section in Domain 1 at 09:00 UTC, the location indicated by the orange line in Fig. 5.5. Relative humidity [%] (shaded) and horizontal wind speed [ms^{-1}] (black solid lines, contour spacing: 1 ms^{-1}. The black shading represents topography, as resolved by the model

The vertical distribution of EPV and Θ_e (Fig. 5.7a) shows slightly negative values of EPV in the order of -1 PVU between 3 and 4 km above the area of interest, corresponding to a distinct negative gradient in Θ_e in the same area, indicating potential instability. The vertical distribution of EPVs (Fig. 5.7b) shows a narrow zone of slightly negative values at approximately 4 km above the area of interest.

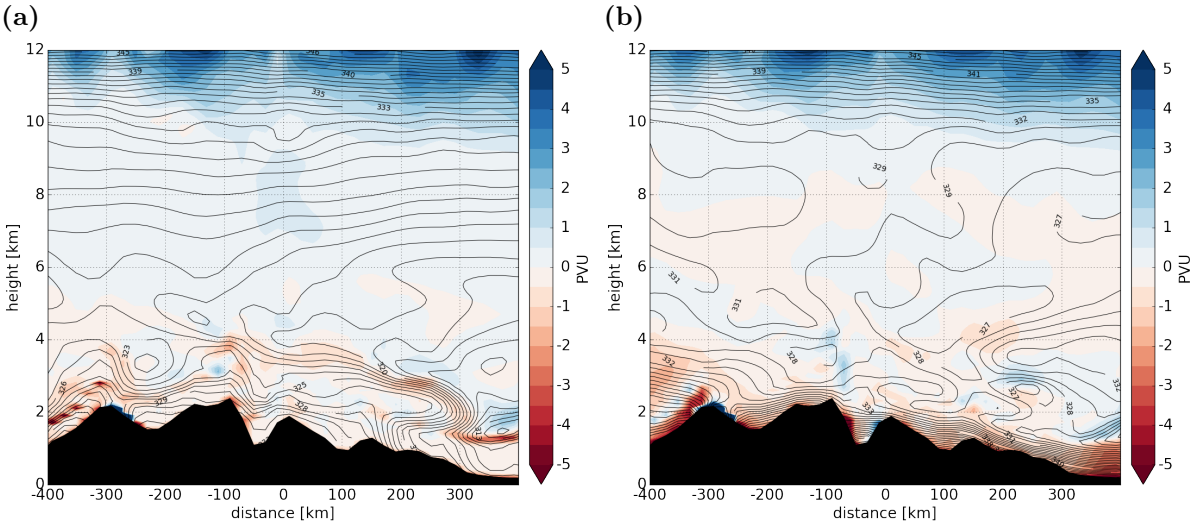

Figure 5.7: West-east vertical cross section in Domain 1 at 09:00 UTC, the location indicated by the orange line in Fig. 5.5. (a) EPV [PVU = 10^{-6}Km^{2}kg^{-1}s^{-1}] (shaded) and equivalent potential temperature [K] (black solid lines), (b) EPVs [PVU] (shaded) and saturated equivalent potential temperature [K] (black solid lines).

5.2.2 Convective Initiation

Analysis of the near-surface parameters potential temperature and water vapour mixing ratio is presented in Fig. 5.8. Deep convection was mainly initiated within the considered section around 10°E and 12°E. The surface moisture distribution indicates mixing ratios of 7-8 gkg^{-1} within the considered area while some of the surroundings contain higher mixing ratios with values up to 12 gkg^{-1}. By 08:00 UTC a slight increase in both potential temperature and water vapour mixing ratio can be noticed. Two hours later, the potential temperature in the considered area has increased by approximately 2 K while an increase in near-surface mixing ratio in the southern part of the area of interest of 2 gkg^{-1} can be detected.

The distribution of CAPE is shown in Fig. 5.9. CIN is not shown in this case as it is almost zero in the area of interest. From 09:00 to 11:00 CAPE values are increasing from < 500 Jkg^{-1} to 500 - 1000 Jkg^{-1}. This coincides with an increase in water vapour mixing ratio within this period.

Compared to the satellite imagery (Fig. 5.2), convection is much more widespread in the model (Fig. 5.10). Signals of maximum radar reflectivity are found over western Austria, Northern Italy and eastern parts of Switzerland. While the first initiation of DMC seems to be related to a certain point at the UTMG in the satellite imagery (Fig. 5.2c), i.e. around 12°E, the convective development simulated by the model shows a more complex distribution. At 12:00 UTC the model indicates a growing of the cells in terms of enhanced signals in the radar reflectivity, mainly around 10°E and 12°E.

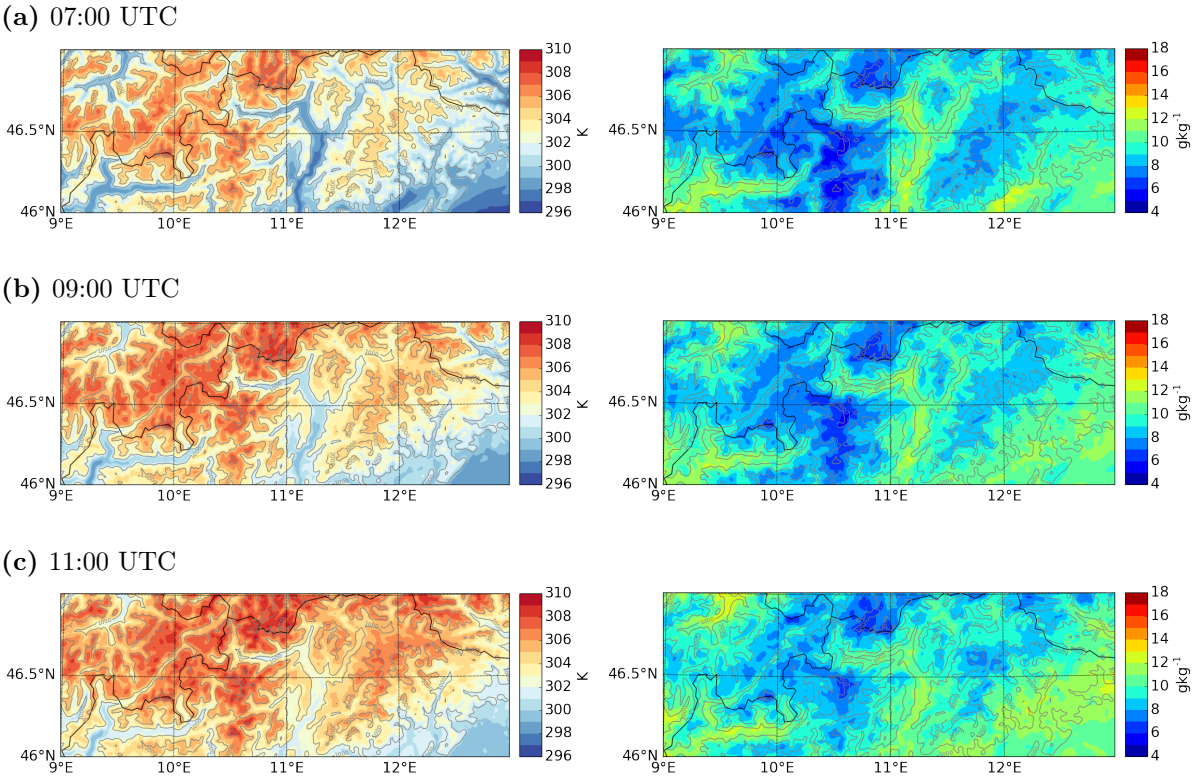

Figure 5.8: Pre-storm conditions in Domain 3. The figure shows the spatio-temporal evolution of near-surface potential temperature (left) and near-surface water vapour mixing ratio (right) at 07:00, 09:00 and 11:00 UTC on 21 July 2013. Grey contours indicate topography (500 m contour spacing)

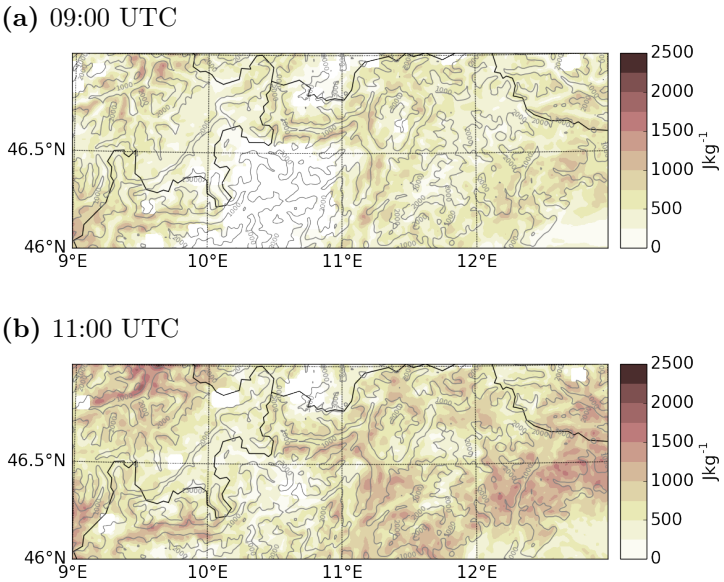

Figure 5.9: Spatio-temporal evolution of CAPE in Domain 3. Grey contours indicate topography (500 m contour spacing)

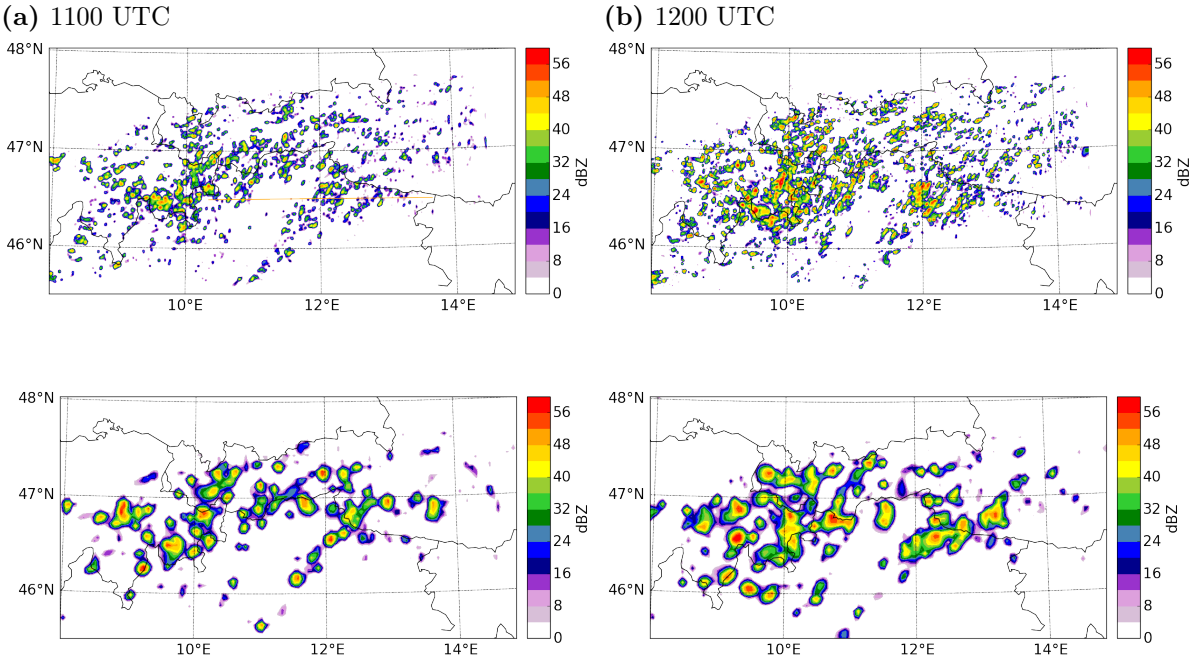

Figure 5.10: Maximum radar reflectivity for Domain 3 (above) and Domain 2 (below) at (a) 11:00 and (b) 12:00 UTC

5.2.3 Transition from shallow to deep convection

The transition from shallow to deep moist convection is shown in the figures below, which represent vertical cross sections of q_{total} and Θ_e (Fig. 5.11) and q_{total} and horizontal wind speed (Fig. 5.12). At 10:00 UTC shallow convective towers, apparently orographically induced, appear over the mountain tops and are capped below heights of approximately 5 km. Negative vertical gradients of Θ_e and vertical wind shear between 2 and 4 km, and therefore below the UTMG, are associated therewith. After one hour of development, at 11:00, the cloud tops have reached heights between 5 and 6 km and finally, at 12:00 UTC, mature deep moist convective development can be detected.

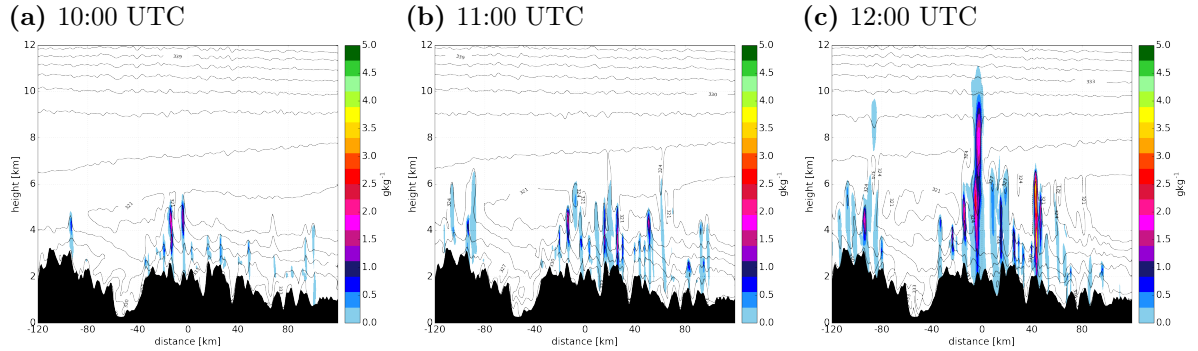

Figure 5.11: West-east vertical cross section of q_{total} (shading) and equivalent potential temperature [K] (black solid lines), 120 km left and right of the considered area, computed in Domain 3. Topography is represented by black shadings.

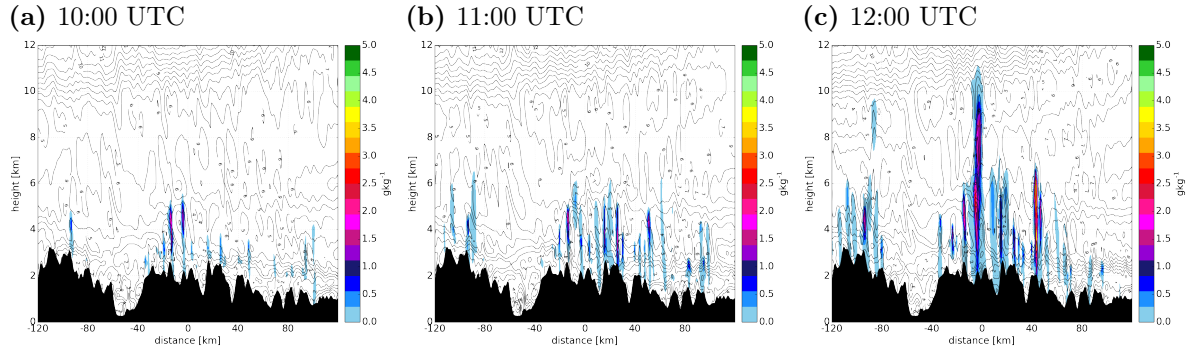

Figure 5.12: West-east vertical cross section of q_{total} (shading) and horizontal wind speed [ms^{-1}] (black solid lines) computed in Domain 3. The location of the cross-section is indicated by an orange line in Fig. 5.10

Investigating temperature and dew-point temperature in a skew-T log-p diagram at 07:00 and 10:00 UTC (5.13) yields that there is no capping inversion or lid hindering the convective development. Also, the drying of the atmosphere at 400 hPa at 10:00 UTC is visible.

A time-height cross-section of relative humidity and wind speed shows the evolution of deep moist convection in Domain 2 (5.14). The humidity decrease in upper levels is clearly evident as well as high values of relative humidity between 2 and 4 km. Between 10:00 and 11:00 UTC, the transition from shallow to deep convection is visible, accompanied by increased gradients in wind speed.

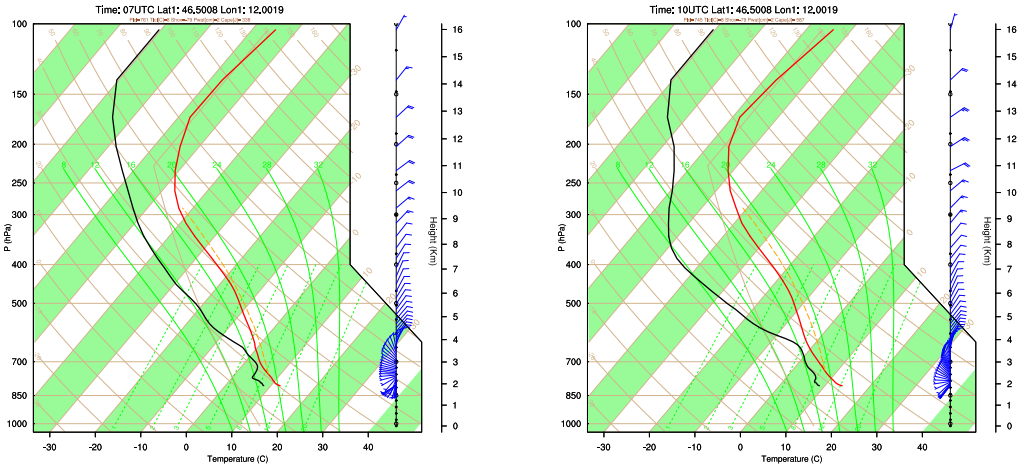

Figure 5.13: Skew-T log-p diagram a 07:00 an 10:00 UTC on 21 July 2013

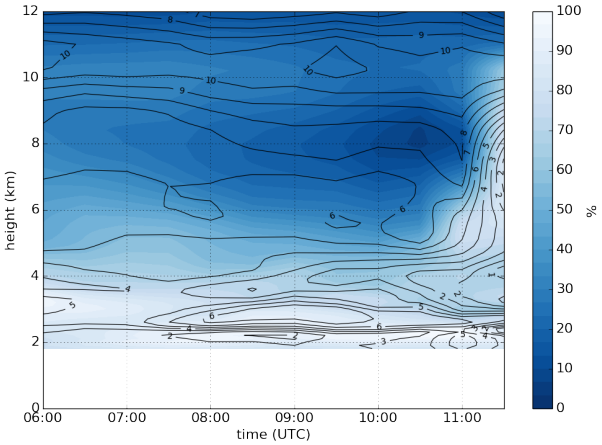

Figure 5.14: Evolution of deep moist convection in Domain 2: time-height cross-section of relative humidity and wind speed [ms^{-1}] at the location where convection was initiated

5.2.4 Indicators for MSI

For assessing the potential of slantwise convection, SCAPE and EPV have been analysed (Fig. 5.15 and 5.16). It can be shown that large parts of the section are characterized by high SCAPE. However, the largest values are found north and south of the area related to convective initiation, leading to the assumption that SCAPE had no significant influence on the convective initiation. The horizontal distribution of minimum EPV and EPVs indicate slightly negative values within the area of interest, although weaker compared to the previous case study.

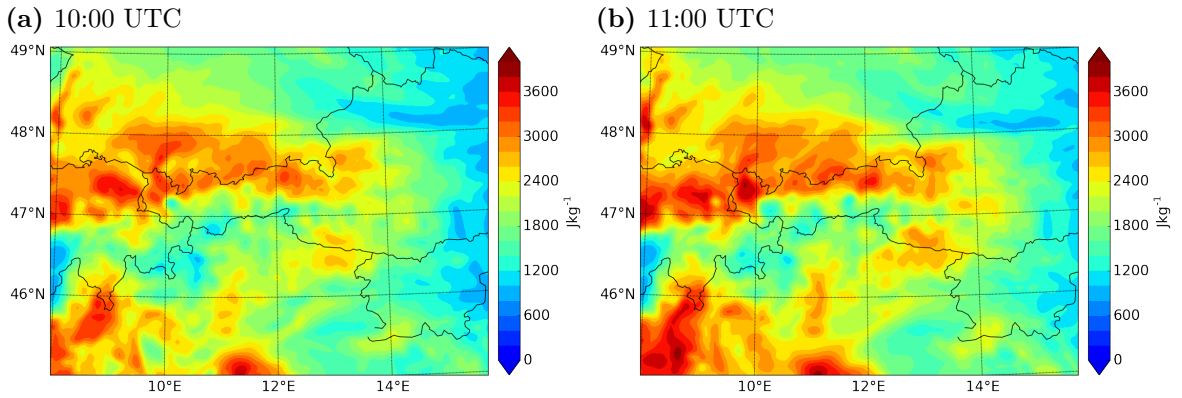

Figure 5.15: SCAPE in Domain 2 at 10:00 UTC and 11:00 UTC

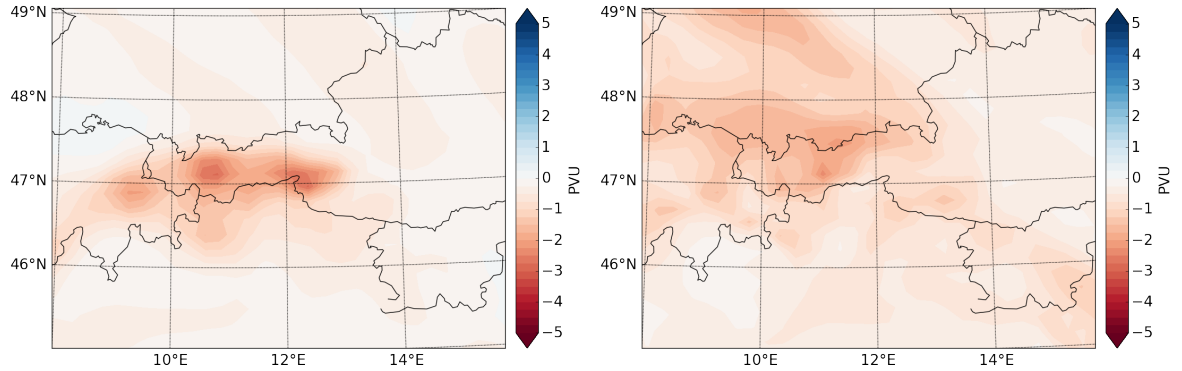

Figure 5.16: Distribution of minimum EPV (left) and EPVs (right) between 700 and 550 hPa in Domain 1 at 10:00 UTC (left)

Chapter 6

Summary and Conclusion

The relation of the initiation of DMC and a corresponding UTMG has been analysed for two representative case studies on 7 July 2014 and 21 July 2013, respectively, with WRF hindcast simulations. Various parameters related to different types of instabilities were calculated from the model output. The simulation was performed with three one-way nested domains with horizontal grid spacings of 20 km (Domain 1), 4 km (Domain 2), and 800 m (Domain 3). The main model results are summarized:

In case study 1 the synoptic conditions are marked by a pressure ridge and shallow convection over the Eastern Alpine region, describing a fair-weather situation - a criterion for the selection of cases. The modelled distribution of the relative humidity at 300 hPa indicates an UTMG in agreement to the satellite imagery.

- The area in the vicinity of the UTMG is characterized by gradients in horizontal wind speed, resulting in vertical wind shear along the boundary of the dry intrusion. Similarly, Antonescu et al. (2013) measured a strong vertical wind shear in conjunction with a tropopause fold. In a time-height cross-section, increasing vertical wind shear can be found in lower levels, prior to the initiation of DMC. Additionally there is an increase in potential temperature and water vapour mixing ratio after the passage of the UTMG. It appears that the UTMG and its characteristics provide the environment for supporting the initiation of DMC.
- Deep moist convection, following widespread shallow convection over mountainous terrain, is reasonably well resolved by Domain 2 and Domain 3 in comparison to satellite and radar imagery. The first transition from shallow to deep convection takes place in the vicinity of the UTMG, as expected. Furthermore, the DMC development is characterized by horizontal and vertical gradients of Θ_e and horizontal wind speed. A sensitivity test for three different microphysics schemes (WSM6, Thompson and Milbrandt-Yau) reveals that the largest model rainfall is produced by the Thompson scheme, followed by WSM6 and Milbrandt-Yau, both in Domain 2 and 3. The storm structure is similar for all three microphysics schemes in Domain 2 with small differences in the magnitude of radar reflectivity, while the structure for Domain 3 is more complex, consisting of more isolated cells.
- A detailed analysis of the model output in Domain 3 yields that a convergence line may have had a role in triggering convection, as its position coincides well with the area of deep convective initiation. The type of convective initiation mechanism in relation to the dry

intrusion resembles the CSIP case study described by Russell et al. (2009) in a way that both convergence and a dry intrusion can be connected to promote DMC in the light of the previously mentioned hypotheses.

- Analysis of diagnostic parameters relevant for MSI yields that the area of interest is characterized by minima of EPV and EPVs between 750 and 600 hPa. Additionally, an area of high SCAPE, also an indicator for CSI, can be found within the same area. The lack of detailed knowledge of SCAPE makes an interpretation of these values challenging. Apart from that, the magnitude of SCAPE values is remarkably high (with maxima up to 4000 Jkg^{-1}), considering that Schultz and Schumacher (1999) referred to SCAPE as typically being small in comparison to CAPE, when CAPE is zero or small.

- From the parcel trajectory analysis it was shown that the vertical wind component w dominates the horizontal wind components u and v at any time within the convective updraught. A complicating factor here concerns the magnitude of the convective updraughts, which are assumed to be much weaker for slantwise circulations (in the order of tens of cms^{-1} compared to gravitational convection, where updraughts are often exceeding 5 ms^{-1}) (Schultz and Schumacher, 1999, p. 2721). The calculation of accelerations along the trajectory, which would help enabling a better differentiation between the two types of instabilities, was not done for this study and remains a task for future work.

- EPV, as a diagnostic tool for MSI, is also used to identify regions of moist gravitational instabilities which leads to the fact that a distinction between these instabilities is not straightforward. An identification of MSI based on the $\overline{\mathrm{M}} - \overline{\Theta}_{\mathrm{e}}^{*}$ or $\overline{\mathrm{M}} - \overline{\Theta}_{\mathrm{e}}$ relationship would require several assumptions that are not strictly met in this particular case (see section 2.1.5). Previous literature often deals with idealized simulations or with simulations under preferred conditions which makes the assessment of symmetric instabilities clearer (e.g. Morcrette and Browning (2006), Fantini et al. (2012)). Furthermore, many previous case studies are dealing with CSI as an explanation for banded precipitation while little research was conducted in connection to the distinction between gravitational and symmetric instability as well as their coexistence. In this context, it should be mentioned that the model resolution (horizontal and vertical) might be a limiting factor in simulating MSI adequately (Schultz and Schumacher, 1999, p. 2724).

- As mentioned by Schultz and Schumacher (1999), areas prone to CSI may occur close to a gravitationally unstable environment. Under these conditions, the resulting convection may consist of slantwise or gravitational convection or both. Furthermore, it is possible that they change from one state into another. This particularly complicates the distinction between the release of these two types of instabilities in an environment susceptible to both of them.

- A hypothesis dealing with atmospheric lids was proposed in Chapter 3. From the model results it seems that, apart from a morning capping inversion at 850 hPa which had been

removed quickly, no atmospheric lid had a notable influence on the initiation of DMC. Despite that, the influence of UTMGs on capping inversions shall be subject of future investigations.

- Another hypothesis was formulated concerning the spatial variability of diabatic heating in relation to moisture gradients in the mid or upper tropospheric levels. Investigation of (potential) temperature surface fields showed no clear signal that could be brought in line with the UTMG (not shown). Therefore, it can be concluded that the influence of the UTMG regarding spatial variability of surface heating is negligible in this case.
- Another aspect that might need to be considered when analysing DMC in relation to the UTMG is the effect of entrainment. If there is insufficient moisture in lower levels, a dry mid- or upper troposphere may hinder a further development of DMC by causing evaporation and therefore negative buoyancy. Future model simulations might enlighten this aspect.

In case study 2 the synoptic conditions are marked by a pressure ridge over Europe and shallow convection over the Alpine region, describing a fair-weather situation. Also in this case, a UTMG is present in the model - in agreement to the satellite imagery - and is marked by a dark stripe in relative humidity with it's most distinctive appearance at 400 hPa. Compared to the previous case study, the horizontal gradients as well as the vertical extent are less distinct. The initiation of DMC occurs in very complex terrain, which may include other relevant mechanisms, not investigated in this study.

- Also in this case, a vertical gradient in wind speed can be found close to the boundary of the dry intrusion.
- Deep moist convection is resolved by Domain 2 and Domain 3, although it appears much more widespread in comparison to the satellite imagery. Also, the first initiation of DMC can not be strictly connected to the UTMG and doesn't match the position in the satellite images.
- The ingredients for MSI are significantly weaker in this case, where in the area of convection initiation SCAPE values are much smaller than in the surrounding area. Also, the horizontal and vertical distribution of minima of EPV and EPVs within the area of interest does not show definite signals with values being weaker compared to case 1. In contrast to case 1, MSI indicators can not be clearly linked to the onset of DMC, perhaps due to the dominating role of factors like low level convergences.

Generally, it could be shown that, especially in case 1, the UTMG seems to support the initiation of deep moist convection. An explicit distinction between the contribution of moist symmetric and moist gravitational instabilities has proved difficult and remains subject of further investigation. Performing experiments with idealized simulation might help to gain a better understanding of MSI contributing to the initiation of DMC under the aforementioned conditions.

Bibliography

American Meteorological Society (2016a), 'convection' - AMS glossary. URL: `http://glossary.ametsoc.org/wiki/convection`.

American Meteorological Society (2016b), 'instability' - AMS glossary. URL: `http://glossary.ametsoc.org/wiki/instability`.

Antonescu, B., G. Vaughan, and D. M. Schultz (2013), A five-year radar-based climatology of tropopause folds and deep convection over wales, united kingdom. *Monthly Weather Review* **141**, 1693–1707.

Appenzeller, C., H. Davies, and W. Norton (1996), Fragmentation of stratospheric intrusions. *Journal of Geophysical Research: Atmospheres* **101**, 1435–1456.

Bennetts, D. and J. Sharp (1982), The relevance of conditional symmetric instability to the prediction of mesoscale frontal rainbands. *Quarterly Journal of the Royal Meteorological Society* **108**, 595–602.

Browning, E. K. (1976), The marginal cost of public funds. *The Journal of Political Economy* pp. 283–298.

Browning, K. (1993), Evolution of a mesoscale upper tropospheric vorticity maximum and comma cloud from a cloud-free two-dimensional potential vorticity anomaly. *Quarterly Journal of the Royal Meteorological Society* **119**, 883–906.

Browning, K. (1997), The dry intrusion perspective of extra-tropical cyclone development. *Meteorological Applications* **4**, 317–324.

Browning, K. A., A. M. Blyth, P. A. Clark, U. Corsmeier, C. J. Morcrette, J. L. Agnew, S. P. Ballard, D. Bamber, C. Barthlott, L. J. Bennett, et al. (2007), The convective storm initiation project. *Bulletin of the American Meteorological Society* **88**, 1939.

Byers, H. R. and R. R. Braham (1949), *The thunderstorm: report of the Thunderstorm Project*. US Government Printing Office.

Chen, F., K. Mitchell, J. Schaake, Y. Xue, H.-L. Pan, V. Koren, Q. Y. Duan, M. Ek, and A. Betts (1996), Modeling of land surface evaporation by four schemes and comparison with fife observations. *Journal of Geophysical Research: Atmospheres* **101**, 7251–7268.

Dixon, R. S. (1999), *Diagnostic studies of symmetric instability*. Ph.D. thesis, University of Reading.

Doswell III, C. A. (1987), The distinction between large-scale and mesoscale contribution to severe convection: A case study example. *Weather and Forecasting* **2**(1), 3–16.

Dotzek, N., P. Groenemeijer, B. Feuerstein, and A. M. Holzer (2009), Overview of essl's severe convective storms research using the european severe weather database eswd. *Atmospheric research* **93**, 575–586.

Dudhia, J. (1989), Numerical study of convection observed during the winter monsoon experiment using a mesoscale two-dimensional model. *Journal of the Atmospheric Sciences* **46**, 3077–3107.

Emanuel, K. (1980), Forced and free mesoscale motions in the atmosphere. In: *Proceedings of CIMMS Symposium (YK Sasaki, N. Monji, and S. Bloom, Ed s.). Norman, OK*, pp. 191–259.

Emanuel, K. A. (1983), On assessing local conditional symmetric instability from atmospheric soundings. *Monthly weather review* **111**, 2016–2033.

Fantini, M., P. Malguzzi, and A. Buzzi (2012), Numerical study of slantwise circulations in a strongly sheared prefrontal environment. *Quarterly Journal of the Royal Meteorological Society* **138**, 585–595.

Fawbush, E. and R. Miller (1952), A mean sounding representative of the tornadic airmass environment. *Bull. Amer. Meteor. Soc* **33**, 303–307.

Gray, S. L. and A. Thorpe (2001), Parcel theory in three dimensions and the calculation of SCAPE. *Monthly weather review* **129**, 1656–1672.

Graziano, T. M. and T. N. Carlson (1987), A statistical evaluation of lid strength on deep convection. *Weather and Forecasting* **2**, 127–139.

Holton, J. R. and G. J. Hakim (2012), *An introduction to dynamic meteorology*, vol. 88. Academic press.

Hong, S.-Y. and J.-O. J. Lim (2006), The WRF single-moment 6-class microphysics scheme (WSM6). *J. Korean Meteor. Soc* **42**, 129–151.

Hoskins, B. (1974), The role of potential vorticity in symmetric stability and instability. *Quarterly Journal of the Royal Meteorological Society* **100**, 480–482.

Hoskins, B. J., M. McIntyre, and A. W. Robertson (1985), On the use and significance of isentropic potential vorticity maps. *Quarterly Journal of the Royal Meteorological Society* **111**, 877–946.

Janjić, Z. I. (2002), Nonsingular implementation of the mellor–yamada level 2.5 scheme in the ncep meso model. *NCEP office note* **437**, 61.

Kirshbaum, D. J. (2011), Cloud-resolving simulations of deep convection over a heated mountain. *Journal of the Atmospheric Sciences* **68**, 361–378.

Krennert, T., A. Kainz, and S. Serafin (2015), An extended perspective for DMC initiation in the alpine region? .

Krennert, T. and V. Zwatz-Meise (2003), Initiation of convective cells in relation to water vapour boundaries in satellite images. *Atmospheric research* **67**, 353–366.

Lim, J.-O. J. and S.-Y. Hong (2005), Effects of bulk ice microphysics on the simulated monsoonal precipitation over east asia. *Journal of Geophysical Research: Atmospheres* **110**(D24).

Lin, Y.-L. (2007), *Mesoscale dynamics*. Cambridge University Press.

Liou, K.-N. (2002), *An introduction to atmospheric radiation*, vol. 84. Academic press.

Markowski, P. and Y. Richardson (2011), *Mesoscale meteorology in midlatitudes*, vol. 2. John Wiley & Sons.

McCann, D. W. (1995), Three-dimensional computations of equivalent potential vorticity. *Weather and forecasting* **10**, 798–802.

Mellor, G. L. and T. Yamada (1982), Development of a turbulence closure model for geophysical fluid problems. *Reviews of Geophysics* **20**(4), 851–875.

Milbrandt, J. and M. Yau (2005), A multimoment bulk microphysics parameterization. part I: Analysis of the role of the spectral shape parameter. *Journal of the atmospheric sciences* **62**, 3051–3064.

Mlawer, E. J., S. J. Taubman, P. D. Brown, M. J. Iacono, and S. A. Clough (1997), Radiative transfer for inhomogeneous atmospheres: RRTM, a validated correlated-k model for the longwave. *Journal of Geophysical Research: Atmospheres* **102**, 16663–16682.

Morcrette, C. and K. Browning (2006), Formation and release of symmetric instability following Delta-M adjustment. *Quarterly Journal of the Royal Meteorological Society* **132**, 1073–1089.

Neiman, P. J., M. Shapiro, and L. Fedor (1993), The life cycle of an extratropical marine cyclone. part II: Mesoscale structure and diagnostics. *Monthly weather review* **121**, 2177–2199.

Orlanski, I. (1975), A rational subdivision of scales for atmospheric processes. *Bulletin of the American Meteorological Society* **56**, 527–530.

Russell, A., G. Vaughan, E. Norton, C. Morcrette, K. Browning, and A. Blyth (2008), Convective inhibition beneath an upper-level PV anomaly. *Quarterly Journal of the Royal Meteorological Society* **134**, 371–383.

Russell, A., G. Vaughan, E. G. Norton, H. Ricketts, C. J. Morcrette, T. J. Hewison, K. BROWNING, A. M. Blyth, et al. (2009), Convection forced by a descending dry layer and low-level moist convergence. *Tellus A* **61**, 250–263.

Schultz, D. M. and P. N. Schumacher (1999), The use and misuse of conditional symmetric instability. *Monthly Weather Review* **127**, 2709–2732.

Seman, C. (1992), On the role of nonlinear convective-symmetric instability in the evolution of a numerically simulated mesoscale convective system. In: *Preprints, 5th Conference on Mesoscale Processes, Atlanta, GA, Amer. Meteor. Soc*, pp. 282–287.

Seman, C. J. (1991), Numerical study of nonlinear convective-symmetric instability in a rotating baroclinic atmosphere .

Shutts, G. (1990), SCAPE charts from numerical weather prediction model fields. *Monthly weather review* **118**, 2745–2751.

Skamarock, W., J. Klemp, J. Dudhia, D. Gill, D. Barker, M. Duda, X. Huang, W. Wang, and J. Powers (2008), A description of the advanced research WRF version 3, NCAR tech note NCAR/TN 475 STR, 125 pp. *Available from: UCAR Communications, PO Box* **3000**.

Stohl, A. (1998), Computation, accuracy and applications of trajectoriesâĂŤa review and bibliography. *Atmospheric Environment* **32**, 947–966.

Tewari, M., F. Chen, W. Wang, J. Dudhia, M. LeMone, K. Mitchell, M. Ek, G. Gayno, J. Wegiel, and R. Cuenca (2004), Implementation and verification of the unified NOAH land surface model in the WRF model. In: *20th conference on weather analysis and forecasting/16th conference on numerical weather prediction*, pp. 11–15.

Thompson, G., P. R. Field, R. M. Rasmussen, and W. D. Hall (2008), Explicit forecasts of winter precipitation using an improved bulk microphysics scheme. part II: Implementation of a new snow parameterization. *Monthly Weather Review* **136**, 5095–5115.

University of Wyoming (2016), Wyoming weather web - atmospheric soundings. URL: `http://weather.uwyo.edu/upperair/sounding.html`.

Xu, Q. (1986), Conditional symmetric instability and mesoscale rainbands. *Quarterly Journal of the Royal Meteorological Society* **112**, 315–334.

List of Tables

List of Figures

List of Symbols

b	buoancy [m^3kg^{-1}]
c_p	heat capacity for constant pressure [$Jkg^{-1}K-1$]
η_g	geostrophic absolute vorticity [PVU]
f	Coriolis parameter
g	gravitational acceleration [ms^{-1}]
L	latent heat of condensation [Jkg^{-1}]
M_g	component of absolute geostrophic momentum [ms^{-1}]
N_g	component of absolute geostrophic momentum [ms^{-1}]
M_0	component of absolute geostrophic momentum at 950 hPa [ms^{-1}]
N_0	component of absolute geostrophic momentum at 950 hPa [ms^{-1}]
N	Brunt-Väisälä frequency
N_m	saturated moist Brunt-Väisälä frequency
γ	environmental lapse rate [K^{-1}]
Γ_d	dry adiabatic lapse rate [K^{-1}]
Γ_s	saturated adiabatic lapse rate [K^{-1}]
p	pressure [hPa]
q_d	total water mixing ratio [gkg^{-1}]
q_{vs}	water vapour saturation mixing ratio [gkg^{-1}]
R_d	ideal gas constant [$Jkg^{-1}K^{-1}$]
T	temperature [K]
Θ	potential temperature [K]
Θ_e	equivalent potential temperature [K]
Θ_{es}	saturated equivalent potential temperature [K]
Θ_w	wetbulb potential temperature [K]
u_g	geostrophic wind component in x-direction [ms^{-1}]
v_g	geostrophic wind component in v-direction [ms^{-1}]
u	wind component in x-direction [ms^{-1}]
v	wind component in v-direction [ms^{-1}]

w	wind component in z-direction [ms^{-1}]

List of Acronyms

AMS	American Meteorological Society
CAPE	Convective Available Potential Energy
CIN	Convective Inhibition
CSIP	Convective Storm Initiation Project
CI	Conditional Instability
CSI	Conditional Symmetric Instability
DMC	Deep Moist Convection
ECMWF	European Centre for Medium-Range Weather Forecasts
EPV	Equivalent Potential Vorticity
EPV_s	Saturated Equivalent Potential Vorticity
ESSL	European Severe Storms Laboratory
ESWD	European Severe Weather Database
LFC	Level of Free Convection
LCL	Lifting Condensation Level
LNB	Level of Neutral Buoyancy
MAXCAPPI	MAXimum Constant Altitude Plan Position Indicator
MSI	Moist Symmetric Instability
MSG	Meteosat Second Generation
PI	Potential Instability
PSI	Potential Symmetric Instability
PV	Potential Vorticity
PVU	Potential Vorticity Unit
RGB	Red Green Blue
RH	Relative Humidity
SCAPE	Slantwise Convective Available Potential Energy
UTMG	Upper Tropospheric Moisture Gradient

WV	Water Vapour
WRF	Weather Research and Forecasting
ZAMG	Zentralanstalt für Meteorologie und Geodynamik